

Università degli Studi Roma Tre



SCUOLA DI DOTTORATO

Dottorato in Ingegneria Meccanica e Industriale – XXII ciclo

Statistical properties of attached and separated wall flows

Aloisio Giovanni

A.A. 2007/2011

Docente Guida: Prof. Roberto Camussi

1 Introduction	4
2 Background concepts	7
2.1 <i>Physical aspects: Attached turbulent boundary layer (TBL)</i>	7
2.2 <i>Physical aspects: Forward facing step (FFS)</i>	11
3 Experimental set-up	15
3.1 <i>Experimental set-up for the study of attached Turbulent Boundary Layers</i>	15
3.2 <i>Experimental set-up for the study of the Forward Facing Step (FFS)</i>	21
4 Results	25
4.1 <i>Turbulent Boundary Layer (TBL)</i>	25
4.1.1 Results and comparisons on velocity statistics	25
4.1.2 Results and comparisons on vortical structures.....	35
4.2 <i>Forward Facing Step (FFS)</i>	43
4.2.1 The recirculation region	43
4.2.2 Wall Pressure Statistics	47
4.2.2 Pressure/velocity correlations	67
5 Conclusion	74
5.1 Attached TBL.....	74
5.2 <i>The FFS behaviour</i>	77
6 References.....	80

1 Introduction

The aim of this work is study study of the flow field and wall pressure fluctuations induced by quasi-two-dimensional incompressible turbulent boundary layers overflowing a forward-facing step (FFS).

Preliminary to the study of the FFS flow, our attention is oriented to the characterization of incoming boundary layer. It is a zero pressure gradient turbulent boundary layer at high Reynolds numbers ($Re_\theta = 3940$ and 7257 , based on momentum thickness), and the reason why we study this type of flows is not only to determine the properties of the flow impacting the obstacle but also to validate the experimental set-up and the novel method of investigation adopted in the present approach.

A time-resolved two-dimensional particle image velocimetry measurements is used. The boundary layer is obtained on the flat wall of a very large recirculating water channel available at INSEAN (Istituto Nazionale Per Studi Ed Esperienze Di Architettura Navale) and is investigated on a streamwise-wall-normal plane. Statistical moments of velocity are determined with the aim to analysing high-Reynolds-number effects in profiles obtained in a direction orthogonal to the wall. A careful analysis of the mean velocity profiles for the measured average velocity indicates departures from the classical logarithmic law towards the power law or parametric models. Such a departure seems to be independent on the specific parameters used in model laws.

Instantaneous velocity fields are deeply analysed to derive information on the dynamic processes involving the generation and evolution of near-wall vortical

structures. Different vortex eduction methods are implemented including Reynolds decomposition, vorticity, invariants of velocity gradient tensor and wavelet tools and compared. The agreement of the results achieved with these methods is rather good, so all of them are used to derive information on wall dynamics. Independently of the Reynolds numbers, packets of vortical structures are observed to form and to evolve aligned more or less at an angle of 30° with respect to wall. In order to quantify the importance of such 'coherent' phenomena over the entire range of turbulent structures, probability density functions of the vortical structure size (obtained from wavelet analysis) are determined. The results show the existence of a hierarchical relation between coherent vortices, the average vortex size being almost equal to $1/10$ of the boundary layer displacement thickness. The measured data are consistent with the formation of about seven large 'children' vortices from each 'parent' vortex. After concluding the study of the attached flow of TBL and after have confirmed the goodness of the methodology and the experimental set-up used we went to study the forward facing step flows.

The study of the separated flow is focussed on the statistical characterization of the pressure fluctuations that are measured upstream and downstream of an instrumented FFS step model installed inside a large scale recirculation water tunnel. Two-dimensional (2D) velocity fields are measured as well close to the step via 2D particle image velocimetry (PIV). The overall flow physics is studied in terms of averaged velocity and vorticity fields for different Reynolds numbers based on the step's height. The wall pressure statistics are analyzed in terms of several indicators, including the root mean square and probability density

functions of the pressure fluctuations, demonstrating that the most relevant flow structure is the unsteady recirculation bubble formed at the reattachment region downstream of the step. Pressure spectra and cross correlations are computed as well, and the convection velocity characterizing the propagation of hydrodynamic perturbations is determined as a function of the distance to the vertical side of the step. The simultaneous measurement of time-resolved PIV fields and wall pressure signals enabled us to compute the pressure/velocity cross correlations in the region downstream of the step and substantiated the relevant role played by the recirculation bubble.

2 Background concepts

2.1 Physical aspects: Attached turbulent boundary layer (TBL)

Despite the large amount of work, there are still several open problems in the investigation of near-wall turbulent boundary layers (TBLs). Up to now, both the relatively simple behaviour of the mean streamwise velocity profile and the more complex dynamics of embedded vortical structures are still in some mist (even if some specific aspect has been clarified). Possibly, these arguments, as also the problem of correct scaling in the different wall sub-regions, should be enclosed in a single conceptual view. Concerning the mean streamwise velocity profile, the 'logarithmic' law of the wall was a paradigm of TBL investigations for many years, although not an exact solution and rather derived from dimensional and asymptotic arguments (H.G.K. Schlichting 2000). Recently, this result was questioned theoretically and experimentally: using a large amount of experimental data, the so-called incomplete self-similarity law was conjectured, in which the dependence of the velocity profile on Reynolds number is avoided only asymptotically (G.I. Barenblatt 1993; G.I. Barenblatt et al. 1993). Thus, the velocity profile exhibits 'power' law behaviour and becomes non-dependent on the viscosity only in its outer part of the layer. The argument is strictly linked to the relevance of viscosity both in the inner and in the outer part of the TBL with some differences in comparison to the classical derivation of the logarithmic law of the wall. On the other side, by analyzing data taken at quite large Reynolds numbers, the complete self-similarity law was also proposed by Zagarola et

al.1997-98. In this case, the profile was observed to follow the power law behaviour in the near-wall region and the universal logarithmic law in the external part, with an overlap region at about $y^+ = 500$ (as usual wall variables are made non-dimensional, indicated by +, by using friction velocity $u_\tau = (\tau_w / \rho)^{1/2}$, where τ_w is the wall shear stress and ρ is the fluid density, and kinematic viscosity ν). The complete self-similarity law also well resembles observations that second-order moments of the streamwise velocity in a channel flow show two maxima for Reynolds numbers $Re_D > 2 \times 10^5$ (Morrison et al. 2004). These maxima are located in the viscous sublayer at $y^+ = 15$, where also the production of turbulence kinetic energy is maximum, and at about $y^+ = 500$, almost where the peak in Reynolds shear stress is. These aspects lead the authors to say that when increasing the Reynolds number, the whole profile, not considering the viscous sublayer ($y^+ < 100$), do not depend on viscosity. The consequent debate on these observations has been long and still not solved (Buschmann and et al. 2003 and Procaccia et al. 2008). It is important to point out that possibly there may not be conflict between the two pictures; rather they may represent two views at small and large Reynolds numbers and/or in different wall regions. In this framework, the recent indications for certain wall sub-regions in which the logarithmic law behaves better than the power law and others in which the opposite takes place can be also regarded (Buschmann and et al. 2003). A combined logarithmic–power law has been recently proposed to account for measured velocity profile on a large part of the wall region (Buschmann and et al. 2003). Thus, previous efforts have been devoted to derive an ‘analytical’ law with some free parameter to be determined by comparison with experiments

and numerical simulations (for example the universally well-known von Karman 'constant') if not derived directly from flow motion equations.

Very recently, a different approach has related the law of the wall to momentum, Reynolds stress and turbulent kinetic energy equations with closure model determined by three free parameters (L'vov-Procaccia-Oleksii, or LPO 2008). This model has been well tested in channel and pipe flows, while both the applicability of the model and the values of the parameters are still questioned in TBL, where the external flow boundary conditions, i.e. the outer flow, are completely different. Thus, in comparing this approach to the previous ones it seems very important to consider the effect of high Reynolds numbers (which are usually not tested so extensively) in a virtually zero pressure gradient TBL.

Of course the behaviour of the statistical moments of velocity is derived from the overlapping of several instantaneous velocity fields. These instantaneous fields involve a wide range of vortical structures whose dynamics is extremely complex and interesting. Since the early 1930s, large-scale and coherent motions near the wall have been detected and the presence of hairpin-shaped vortices has been recognized. During the last 15 years, parallel to the debate on the characterization of the TBL mean streamwise velocity profile (and higher-order statistics), there was another debate on the existence of the so-called packets of coherent structures. In particular, the questions are as follows: Which kind of vortical coherent structure characterizes the TBL? How are these structures generated? How are they sustained (or how do they self-sustain)? And moreover if and how do they depend on the Reynolds number? In 1990 Robinson et al. summarized and classified the different kinds of coherent structures with

respect to the position they occupied in the TBL. Hairpin-shaped vortices and related structures were detected only out of the viscous sublayer. After this cornerstone work, thanks to the fast improvements in both numerical and experimental methods, different conceptual models describing vortex dynamics in a TBL have been proposed. Without entering into details, one of these, proposed and upgraded through many papers (consider for example Adrian et al. 2000 and Tomkins et al. 2003), is based on auto-generation and self-sustenance of coherent structures. Hairpin vortices are created by conservation of turbulent energy from the quasi-streamwise vortices positioned in the buffer layer. Turbulent energy itself is then responsible of the generation of two new ‘legs’ when the ‘head’ of the previous vortex moves away from the wall. So far, this continuous process allows the vortices to form the so-called packets. Direct numerical simulation (DNS) predictions and particle image velocimetry (PIV) measurements (up to $Re_\theta = 6845$) agreed in finding these coherent structure packets both near the wall ($y^+=60$) and in the outer layer, developing towards preferential directions forming with the wall itself an angle between 30° and 60° . On the other hand, non-planar spanwise velocity component is important in another model (Jeong et al. 1997), in which ‘legs’ axes form an angle of at least 4° with respect to the streamwise direction on the horizontal plane. These two and other models (for example Perry et al. 1995) consider the ‘coherent’ part of the near-wall dynamics, while not so many efforts have been made in deriving the overall relevance of such part in comparison with the entire TBL dynamics (Camussi et al. 2002). Specifically, two questions are still open:

- (1) What is the dependence of the observed phenomena on Reynolds number?
- (2) What is the effective relevance of the coherent part in comparison with the entire TBL dynamics at high Reynolds numbers?

These two questions are partially linked due to the possible relation between the relevance of the coherent part and the Reynolds number. Therefore, the aim of the present work is to investigate the behaviour of a virtually zero pressure gradient TBL in a large facility so that high Reynolds numbers are obtained. To investigate simultaneously the law of wall open problem (i.e. the velocity statistics) and the wall dynamics, the time-resolved PIV technique is used (i.e. the combination of PIV with the use of high-speed camera). Statistical moments and spatial-time evolution of coherent structures are investigated in order to establish a comparison with literature data and theories and to try to give an answer to previously described open questions.

2.2 Physical aspects: Forward facing step (FFS)

Steps and geometrical irregularities present on surfaces underneath turbulent boundary layers (TBL) induce unsteady dynamic pressure fields which are responsible for a number of phenomena of primary importance in many practical applications, including interior noise generation, flow induced panel vibrations and hydroacoustics of underwater vehicles¹. Despite the fact that most of the studies conducted in the field are related to equilibrium TBL², it is

well known that the presence of flow separations, re-circulations and re-attachments lead to the generation of wall pressure fluctuations whose overall level might be significantly larger (up to 30dB) than that observed in equilibrium TBL with no separations³.

Several studies have been conducted to characterize the fluid dynamic structure of separated flows and the physical mechanisms underlying the development and recovery of the TBL. Detailed results have been obtained for several geometries, including backward facing steps (see Simpson *et al.* 1989 and the literature cited therein for a comprehensive review in the field), sharp edges (as in Kiya & Sasaki, Hudy *et al.*), inclined surfaces and surface bumps. Most of these studies have shown that the wall pressure fluctuations are driven by a low frequency excitation linked to the expansion and contraction of the separation bubble, a phenomenon usually designated as flapping motion. Besides, the vortical structures within the shear layer have been identified as the source of higher frequency peaks normally observed close to the reattachment position.

In contrast, significantly less results are available in the literature for the case of the forward-facing step (FFS), in particular for what concerns the characterization and evolution of the incoming TBL upstream of the step and the induced wall pressure field in the separated region upstream of the surface discontinuity. To this extent, Stürer *et al.* analyzed the separation bubble upstream of a FFS in laminar flow conditions through flow visualizations and particle tracking velocimetry measurements. They demonstrated that the laminar re-circulating region upstream of the step is an open separation bubble characterized by spanwise quasi-periodic unsteadiness. The flow topology and

the pressure field upstream and downstream of an FFS at much higher Reynolds numbers have been recently studied by Largeau & Moriniere. Although the upstream and downstream regions of the FFS are considered, the authors have focused their attention on the latter portion of the flow where the wall pressure statistics have been analysed in great detail. In particular, the effect of the relevant length-scales has been underlined and the influence of the flapping motion upon the pressure field at the reattachment point clearly demonstrated by means of pressure-velocity cross-correlations obtained from simultaneous wall microphones and hot wire anemometry measurements. Fourier pressure spectra upstream and downstream of a FFS have been presented also by Efimtsov *et al.* who showed that the region downstream of the step is the most significant in terms of pressure level. On the other hand, Leclercq *et al.* considered the acoustic field induced by a forward-backward step sequence and suggested that the most effective region in terms of noise emission is located just upstream of the FFS. The experimental results reported in Leclercq *et al.* 2001 have been successfully reproduced in a large eddy simulation performed by the same group. It was confirmed that the largest acoustic source is located in the separated region upstream of the wall discontinuity. In recent papers, Camussi *et al.* measured the pressure fluctuations at the wall of a shallow cavity representing a backward-forward step sequence. The authors again showed that the region close to the FFS is the most effective in terms of wall pressure fluctuations level even though the origin of the observed acoustic field was not clarified.

It is clear that, from the aeroacoustic viewpoint, the FFS geometry is more critical than the BFS case since it induces larger fluctuations in the wall pressure field. However, the physical mechanisms underlying this evidence are not yet fully understood and the results available in the literature are limited and sometimes contradictory. The primary intent of the present work is to cover the lack of experimental results in this field.

An instrumented FFS model has been designed and installed in a large-scale water tunnel where an extensive measurement campaigns has been carried out at different Reynolds numbers based on the step's height, hereafter denoted as Re_h . The overall flow physics have been characterized through time-resolved PIV measurements conducted close to the step. Wall pressure data have been obtained through local measurements performed in several positions upstream and downstream of the step. The main statistical quantities, including root mean squares and probability density functions (PDFs), have been retrieved as well as cross-correlation and power spectra of the unsteady pressure. Simultaneous time-resolved PIV/pressure measurements have also been performed in different flow conditions downstream of the step. Cross-correlations between velocity and pressure have been conducted, primarily to clarify the physical nature of the low frequency pressure fluctuations dominating the spectral energy in the separated regions.

Details about the measurement set-up and the flow conditions are given in the next section together with a comprehensive description of the PIV post-processing technique therein employed.

3 Experimental set-up

The measurements were performed at the INSEAN free-surface large circulating water tunnel. A scheme of the facility is reported in Figure 1. The test section is 10-m long and 3.6-m wide with a depth of 2.25 m. The water flow is driven by two axial pumps requiring a total power of about 900 KW at the maximum water speed of 5.3 m/s.

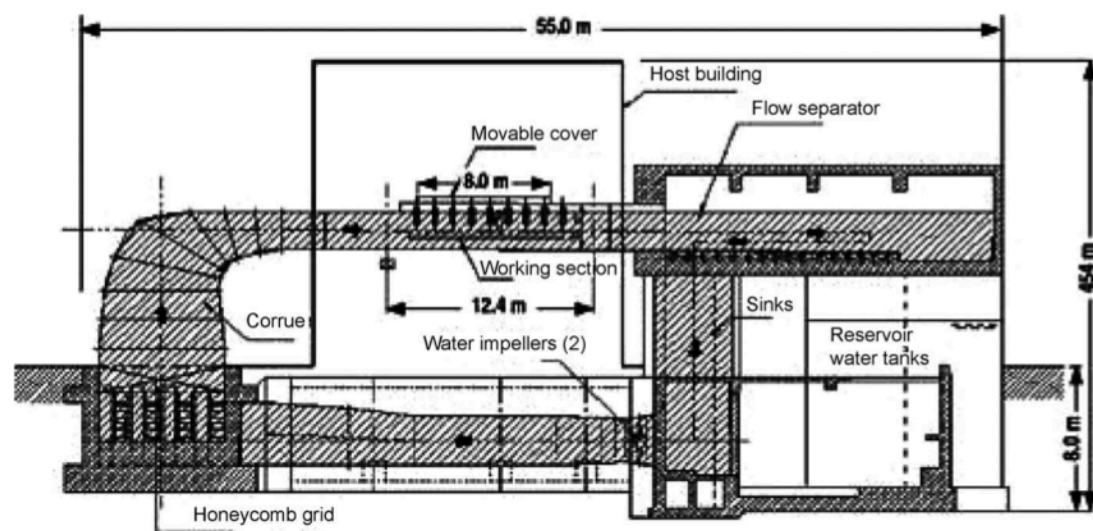


Figure 1 The hydrodynamic circulation channel used for the present experiments.

3.1 Experimental set-up for the study of attached Turbulent Boundary Layers

Measurements have been performed at mean axial velocities (U_∞) equal to 0.5 m/s and 1.05 m/s at the centre of the test section, about 0.6 m below the free surface and 8 m downstream the test section inlet (from where the boundary layer develops). At these velocities the corresponding boundary layer

displacement thicknesses (δ) are 0.16 m and 0.11 m (in good agreement with the TBL theoretical and empirical predictions), resulting Reynolds number values, $Re_\delta = \delta U_\infty/\nu$, equal to about 8×10^4 and 1.2×10^5 respectively. The Reynolds numbers based on the momentum thickness ($Re_\theta = \theta U_\infty/\nu$) are 3940 and 7250 for the two tested velocities, while the Karman numbers ($\delta^+ = \delta 99u_\tau/\nu$) are equal to about 4050 and 6090. The free-surface slope in the channel, if , is equal to about 1/2000.

The time-resolved PIV system consists of a high-speed camera (up to 2000 frames per second at full resolution of 1024×1024 px²), set in a waterproof transparent box partially submerged and facing downward to capture images. The box has two keel-like forward and backward profiles to reduce both vibrations and waves generated at the depth of about 10 cm. The influence of these waves and vibrations on the measurements in the test area was found to be negligible: different immersion depths were tested at far-wall locations, and the differences were well under 1% of the lowest measured streamwise velocity component. A continuous Argon-ion laser (maximum power 5 W and main wavelength 516 nm) was used; the light sheet generated through a system of lens was about 1-mm thick and was positioned perpendicular to the wall, passing through a Perspex window. Different image sizes were acquired in order to investigate statistical properties (as the law of the wall) and the near- wall vortex dynamics: the largest, 65×130 mm² (512×1024 px²), was used to capture the whole boundary layer thickness, while the smallest, 65×65 mm² (1024×1024 px²) was used to acquire more detailed fields for vortical structure detection. The channel water was seeded with hollow glass spheres (density

equal to 1.1 g/cm^3 , refractive index equal to 1.52) with a mean particle diameter of $10 \text{ }\mu\text{m}$. To allow a seeding particle distribution in the boundary layer as homogeneous as possible still minimizing intrusiveness, the glass spheres are injected into the channel 4 m upstream of the measurement volume by a thin cylinder (diameter 1 cm) with 20 holes (diameter 1 mm each) distributed along y^+ . The resulting seeding distribution is quite uniform over about 12 cm (i.e. the whole boundary layer thickness). An example of acquired image is given in Figure 2, where also the wall is visible. Although there are parts of the image with a small number of particles in comparison to the average, the seeding distribution is reasonably homogeneous. (Note that the region on the left side has been truncated due to low laser light.)

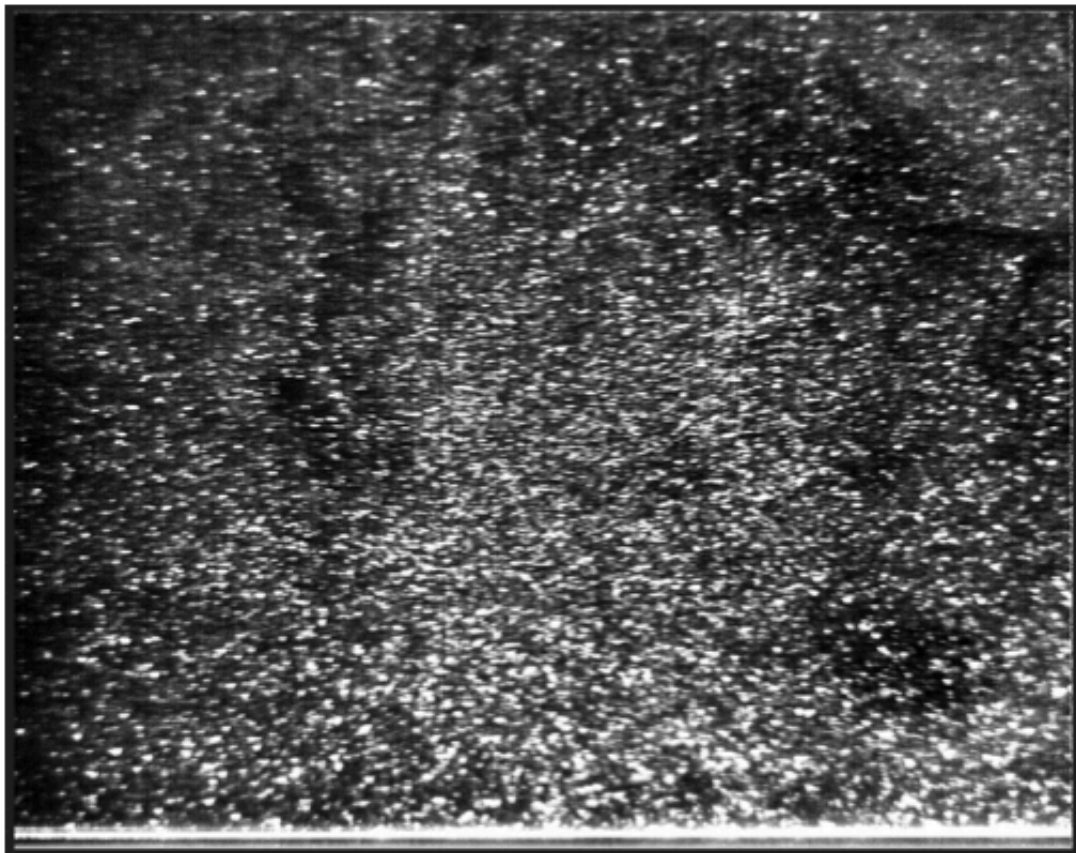


Figure 2 An example of the acquired PIV movie images (2000 frames per second).

PIV image analysis was performed through two steps. The first one involved an iterative window offset fast Fourier transform method in which the sampling grid is continuously refined up to the final interrogation window size. This size was different for the two configurations: the largest images, used to measure the velocity statistics, were analyzed by means of rectangular windows stretched in the direction of the mean flow ($16 \times 32 \text{ px}^2$, 50% overlap), while the smallest were investigated using square windows ($32 \times 32 \text{ px}^2$, 75% overlap), in order to obtain a higher resolution. Window size could not be reduced anymore, as the number of tracer images in each sub-window would decrease considerably and spurious vectors would appear. The second step of the analysis concerned only the smallest images, in order to obtain a better reconstruction of the flow field especially in the regions with strong gradients. These images were actually used to investigate the instantaneous TBL motion and vortical structures, using features of time-resolved PIV. During this second step, images were distorted (as in Huang et al. 1993 following the tracer motion already estimated (by the first step)), to obtain by direct cross-correlation matching a new ‘corrected’ velocity field that, behaving as the new predictor, was ready to deform the original images again. This type of iterative algorithm has been proved to be very efficient, accurate and stable. Synthetic image-based tests were made, in order to verify the improvements achieved: results showed that both mean displacement error and root mean square (rms) error are reduced by about one order of magnitude (Pereira et al. 2004). Also the maximum measurable gradient is increased, bringing us to the possibility of capturing a higher dynamical range, and higher vorticity peaks too. This is very important in the detection of

coherent structures in the boundary layer. For the present PIV images, the image deformation was performed through four iterations with a local Gaussian-weighted filter applied on the predictor field and a Gaussian-based sub-pixel interpolation fit, performed considering 3×3 px2 kernels around the correlation function maxima. The achieved time resolution (5×10^{-4} s) is equal to about 0.2 (low Reynolds number) and 0.8 (high Reynolds number) time wall units ($\Delta t u_\tau^2/\nu$). The spatial separation between velocity vectors (about 0.5 mm) is equal to about 10 and 20 wall units respectively for the two Reynolds numbers. The spatial separation also corresponds to about 50 integral length scales and five Taylor microscales (measured from spatial correlation functions). These values, although non-sufficient to derive the entire spectrum of flow scales, are typical of high-quality PIV investigations in TBLs (Adrian et al. 2000). The number of data used for statistics is equal to about 5×10^5 , which means that the total non-dimensional acquisition time $TU_\infty/\delta > 1000$, i.e. sufficiently good for the evaluation of second-order moments.

The present results obtained with PIV ($Re_\theta = 3940, 7250$) have been compared with the following available model laws or data sets (non-dimensional quantities using inner variables are reported):

- (1) logarithmic law of the wall (H.G.K. Schlichting 2000) $U^+ = C + 1/k \log y^+$;
- (2) power law of the wall (G.I. Barenblatt 1993; G.I. Barenblatt and V.M. Prostokishin 1993) $U^+ = C_p y^{+\alpha}$;
- (3) generalized law of the wall (Buschmann and et al. 2003)
 $U^+ = C + 1/k \log y^+ + B y^+ + E/y^+$

- (4) LPO model (LPO 2008);
- (5) numerical data by DNS simulations on a TBL at $Re_\theta = 300, 700, 1400$ by Spalart (1988);
- (6) experimental data by hot-wire anemometry (HWA) measurements on a TBL at $Re_\theta = 7000$ by Osterlund et al. 2000;
- (7) experimental data by Pitot tube and HWA measurements on a TBL at $Re_\theta = 4980, 7700$ by Smith et al. 1994;
- (8) experimental data by HWA measurements on a turbulent pipe flow at $Re_D = 4.1 \times 10^5$ (Reynolds number based on pipe diameter D) by Morrison et al. 2004.

In the list above, the 'constants' in the models have been changed (as reported in the following sections) except for the generalized law of the wall, where the values obtained from best data fit, $C = 4.9$, $k = 0.41$, $B = 0.001$ and $E = 20$, have been used (Buschmann and et al. 2003).

One of the aims of this work is detection of vortical structures in the TBL to follow them in their evolution in time and space, which is possible due to the use of the time-resolved PIV technique. In order to be sure to have identified effective vortical structures, different detection methods were adopted, including vector fields using Reynolds decomposition, vorticity fields (computed by the Sobel and Kirsch operator Russ et al. 2002), plots of invariants of velocity gradient tensor (Jeong et al. 1995) and local intermittency measure (LIM) wavelet-based fields. In some sense all of them have been used for the purpose: vector decomposed and vorticity fields mainly for comparisons, whereas

invariants of velocity gradient and wavelet tools specifically for vortex detection. Comparisons between these indicators have been made and will be presented in the following sections.

3.2 Experimental set-up for the study of the Forward Facing Step (FFS)

The step's height h has been fixed to 20mm and the spanwise opening was more than 10 times larger than h . As shown in existing literature (e.g. Largeau & Moriniere¹¹), the flow structure upstream of the step is three-dimensional (3D) even though the separation line has been shown to be approximately constant and parallel to the spanwise extension of the discontinuity far from the lateral edges. In the central region, several authors suggest that the flow can be considered two-dimensional (2D) at least in a statistical sense. In this regard, Hoarau et al. 2006 stated that the use of end plates to ensure a two-dimensional flow is not feasible due to the induced disturbances but, without end plates, the flow is 2D in the central region. Other authors (e.g. Moss & Baker, Kiya & Sasaki) confirmed this point and suggested a ratio larger than 10 between the spanwise extension of the step and its height in order to neglect the 3D effects in the central region. This condition is verified in the present work.

The Reynolds number (Re_h) based on h and on the free stream velocity U_0 ranged from 8800 to 26300 and was adjusted by varying U_0 from 0.5m/s to 1.5m/s. The natural boundary layer developing at the wall of the test section has been characterized in a previous work¹⁹ for flow conditions similar to those considered here. The displacement thickness d^* at the model position resulted to be of the order of 10 mm at a free stream velocity of 1m/s.

Wall pressure fluctuations have been measured within a region extending from 6h upstream to 8h downstream of the step. Piezoresistive pressure transducers Endevco 8510B-2 have been flush mounted on the wall. The resonance frequency of the transducers is 70kHz and the diameter size of the measurement surface is 3.8mm, which is less than 40% of the thickness of the boundary layer overflowing the transducer. The effect of the transducer size upon the pressure power spectra reliability has been discussed in several papers, in particular by Bull²⁰ and Corcos²¹. Their main suggestion is that the ratio between the pressure transducer size and the displacement thickness should be approximately lower than 0.5. This criterion is satisfied in the present study. Moreover, the effect of the transducer size would only be relevant at frequencies much larger than the typical range of interest for the separated flow subject of our work. In fact, the Strouhal number St , defined upon the freestream velocity and the step's height, is larger than one. As we shall see in the following sections, the wall pressure dynamics associated to the flow separations and reattachments, either upstream or downstream of the step, are characterized by Strouhal numbers significantly smaller. The transducers have been aligned in the streamwise direction and their separation distance fixed to 15mm, as in D.J.J. Leclercq et al. 13. A schematic of the pressure measurement set-up is reported in Fig. 3.

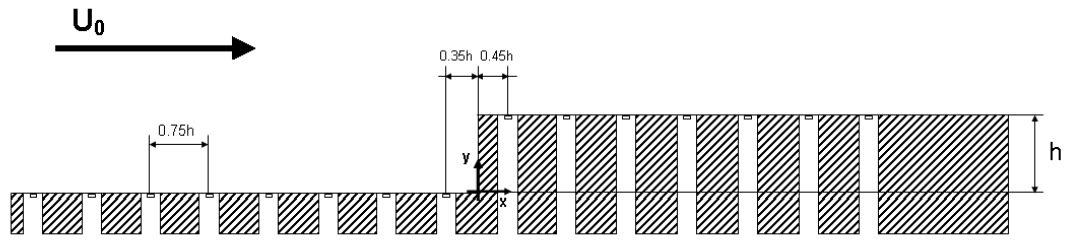


Figure 3 Location of the pressure transducers for the wall pressure measurements. The frame of reference adopted, whose origin is at the step location, and the direction of the free stream velocity are also reported.

Two Brüel&Kjær hydrophones, types 8104 and 8105, have been installed inflow sufficiently far from the instrumented model in order to measure the background noise. In addition, a Brüel&Kjær 4370 accelerometer has been placed close to the step model to monitor the surface vibrations and to check for possible correlations to the pressure fluctuations. Signals have been acquired for 400s, sampled at 1200Hz and preconditioned with an anti-aliasing Butterworth band-pass filter, using a 16-bit 16-channel system (PROSIG P5600).

The PIV measurements were conducted using the time-resolved approach based on the use of a continuous laser source and a high-speed camera. An argon laser source (SPECTRA-PHYSICS Stabilite 2017) emitting a 6W green beam was used to produce a 1mm thick light sheet oriented perpendicular to the wall. The flow was seeded with spherical hollow glass particles having a mean diameter of about 20μm. A schematic view of the experimental set up is reported in Fig. 2. Images were acquired using a high-speed camera (Photron Fastcam APX) capable of a maximum frame rate of 120000fps. The domain of interest was viewed through a mirror mounted on the wall at 45° degrees, as shown in Fig. 4. The mirror was positioned at about 50cm above the measurement area and

carefully aligned with the flow to avoid flow disturbances. The camera is based on a 1024x1024 pixels CMOS sensor, with a pixel size of 17.5 μ m and a 4ms shutter time. For the present acquisitions, the frame rate was 1200fps for an image resolution of 1024x512 pixel². The acquired images were then post-processed using the PIV methodology, based on a standard 2D FFT algorithm combined with the offset correlation and the window deformation techniques. More details on the PIV image processing procedures can be found in Scarano et al. 2002. The size of the final interrogation area was 16x16 pixel² with a 75% overlap between adjacent windows. The spatial resolution of the velocity vectors was in the order of 1mm, which is small enough to resolve the large-scale structures in consideration here, the effective physical size covered by the camera being 160x80 mm². The camera had to be placed at two different locations streamwise to cover the full span of the region of interest. For each Re_h considered, a sequence of 10000 PIV image pairs has been recorded to allow a statistically representative analysis of the velocity field.

For the case $Re_h=17600$, corresponding to $U_0=1$ m/s, time-resolved PIV images in the region downstream of the step and pressure signals from three pressure transducers ($x/h=1.2, 1.95, 2.7$) have been acquired simultaneously at the same sampling rate of 1200Hz. Both images and pressure signals were recorded for 10 seconds as to reach a sufficient statistical convergence.

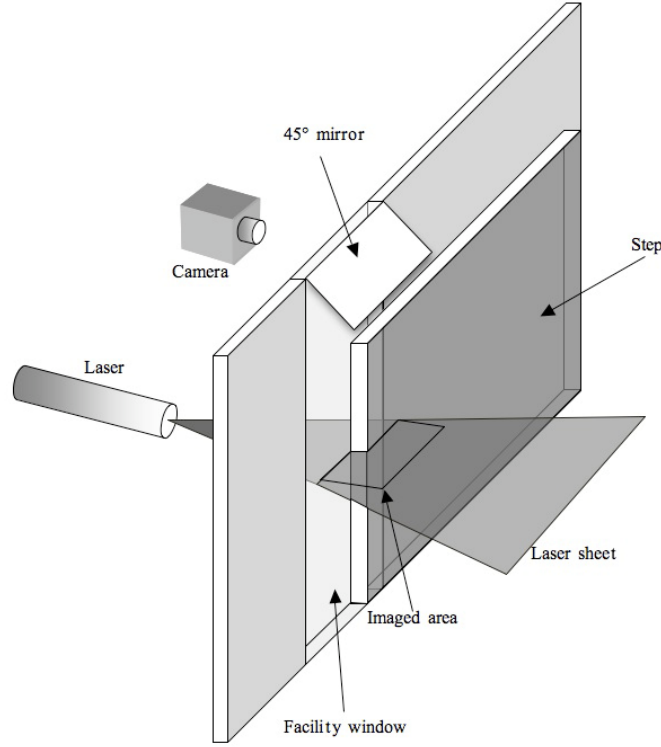


Figure 4 Overall scheme of the step model and the setup for the PIV measurements.

4 Results

4.1 Turbulent Boundary Layer (TBL)

4.1.1 Results and comparisons on velocity statistics

To present non-dimensional results using inner scales, the friction velocity, u_τ , must be evaluated. This determination is quite crucial in TBL investigations; thus different methods have been compared. The first one involves the following equation, used by different authors (see, for example, (G.I.Barenblatt 1993)):

$$u_\tau = \frac{\nu}{x} \left[\frac{e^{\frac{3}{2\varepsilon}} 2^\varepsilon \varepsilon (1 + \varepsilon) (2 + \varepsilon)}{\sqrt{3 + 5\varepsilon}} \right]^{\frac{1}{1+\varepsilon}}, \quad \varepsilon = \frac{3}{2 \ln Re_x}.$$

The original formulation involved Re_D , as it was used for a circular pipe, while here it has been adapted by considering Re_θ , as in the case of a flat plate.

The second evaluation involves the empirical Osterlund formula:

$$u_\tau = U_\infty \left(\frac{c_f}{2} \right)^{1/2}, \quad c_f = 2 \left[\frac{1}{k} \ln Re_\theta + C \right]^{-2}.$$

Differences between friction velocities computed with the two formulas were negligible (2.03 cm/s versus 2.01 cm/s at $U_\infty = 50$ cm/s and 4.03 cm/s versus 3.98 cm/s at $U_\infty = 105$ cm/s).

The third method is the friction velocity measurement from the channel free-surface slope (i.e. compute the wall shear from the momentum balance equation):

$$u_\tau = (g R_h i_f)^{1/2},$$

where R_h is the hydraulic radius. This value is equal to about 5 cm/s for the largest Reynolds number, but in this case the error on free-surface slope is quite large, ± 0.5 mm (25%).

Mean streamwise velocity profiles scaled with inner variables for the two tested Reynolds numbers ($Re_\theta = 3940$ and $Re_\theta = 7250$) are reported in Figure 5. The data well compare with DNS results by Spalart and experimental data by Osterlund et al. 2000 and Smith et al. 1994 (except for the wake region in which Reynolds number effects appear). Even when enlarging the view to the region $y^+ > 100$ (as on the right part of Figure 5) the observed differences are still very small.

Thus, to compare with analytical models it is necessary to amplify the differences.

To this end, the profile of streamwise velocity gradient (along the vertical) is

given in Figure 6 compared with the same data as the previous figure and with logarithmic, power and generalized laws of the wall together with the prediction from the LPO model. All experimental data present some oscillation due to measurement noise (all over the layer) and to limited statistical data set (increasing with y^+ because of the fact that the local integral timescale δ/U is increasing almost linearly with y^+). Moreover, they all agree quite reasonably (especially for $y^+ > 100$), whereas the limited Reynolds number of the DNS simulations causes an evident separation of these data from the others. In comparison with the presented law of the wall models, differences to data are not observed for $y^+ > 300$. It seems that all data and models are quite close to a $1/y^+$ decrease.

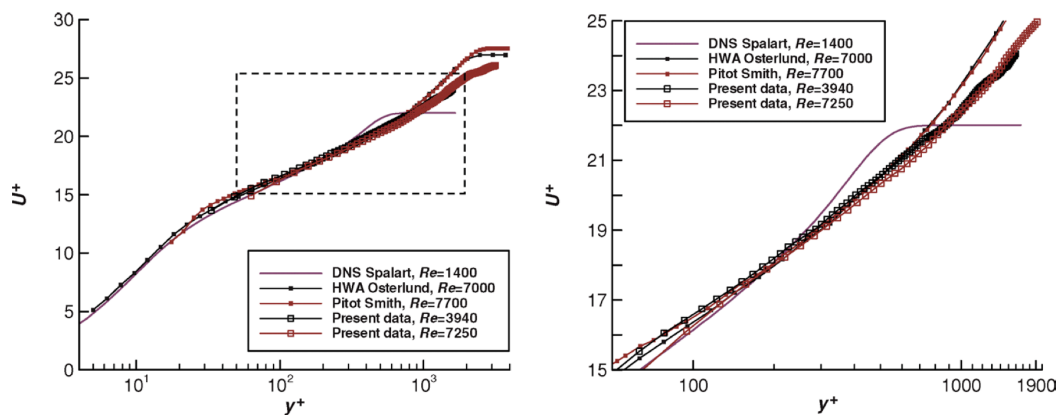


Figure 5 Profiles of non-dimensional (wall variables) streamwise velocity from the present data ($Re_\theta = 3940$ and $Re_\theta = 7250$) compared with the DNS results by Spalart (1988) and the experimental data by Osterlund et al. (2000) and Smith (1994). The dashed region is enlarged on the right.

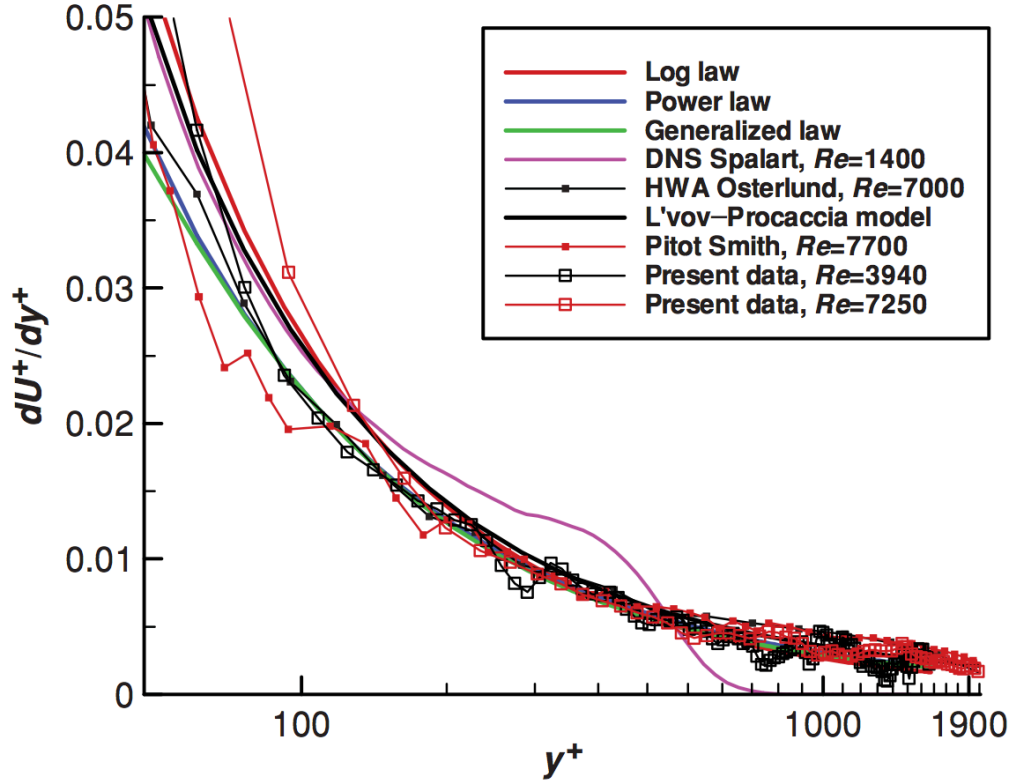


Figure 6 Profiles of non-dimensional (wall variables) streamwise velocity derivative from the present data ($Re_\theta = 3940$ and $Re_\theta = 7250$) compared with the DNS results by Spalart (1988) and the experimental data by Osterlund et al. (2000) and Smith (1994), The logarithmic, power and generalized laws of the wall are overlapped to the data together with prediction from the LPO model.

In particular, it is practically impossible to distinguish between power and generalized laws (that's why the second will be not further considered in the paper), whereas there are much more differences between the logarithmic law, power law and LPO model. In any case it is not possible from this plot to determine which model is better approaching the data. By considering that for the logarithmic law the multiplication of the streamwise velocity gradient along the vertical by y^+ would give a constant (equal to $1/k$), it should be possible to

amplify even more the differences between the data. So far, in Figure 7 the quantity dU^+/dy^+ is plotted dy^+ for the present data (on the left) and for the experimental and numerical data by other authors given in the previous figures (on the right).

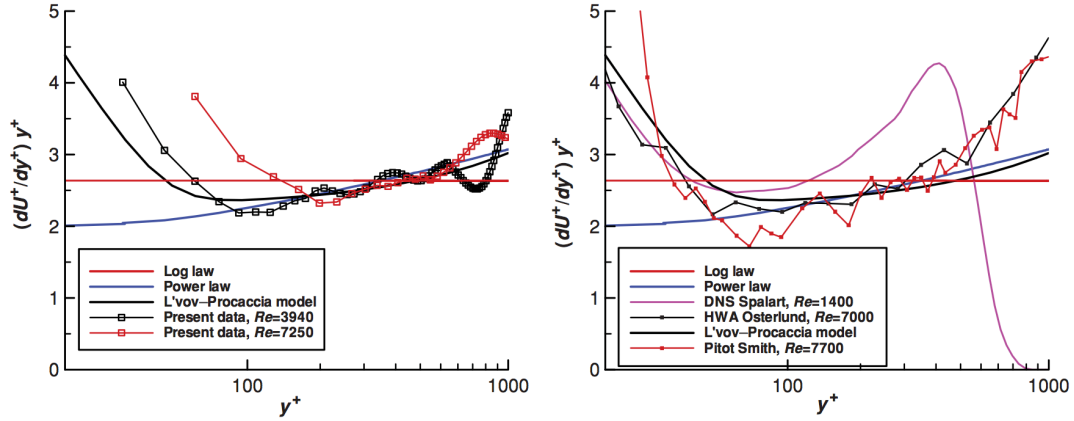


Figure 7 Profiles of $y^*(\partial U^+/\partial y^+)$ from the present data ($Re_\theta = 3940$ and $Re_\theta = 7250$) compared with the logarithmic and power laws of the wall together with the prediction from LPO model (on the left).

The comparison of the same laws and model with the DNS results by Spalart (1990) and the experimental data by Osterlund et al. (2000) and Smith (1994) is given on the right.

Although statistical oscillations are here emphasized by the multiplication by y^+ , some general trend should be derived at least for $y^+ < 1000$. From the analysis of the figures, it is observed that all data show a decreasing behaviour (for $y^+ < 100$), a more or less pronounced minimum ($y^+ \sim 100$) followed by a gradual increase. (The rate seems to be dependent on the Reynolds number.) Thus no constant value is attained, and the logarithmic law seems to be disregarded. On the other hand, the power law model seems to describe reasonably well the behaviour of data (except the DNS data) in the region in which the function dU^+/dy^+ is increasing ($y^+ > 100$). The dy^+ prediction from the LPO model seems the

only one that can account for the observed data behaviour in the entire region $50 < y^+ < 1000$. In any case, from this analysis it is quite clear that the comparison with law of the wall models is very difficult at low Reynolds numbers due to wake effects. Indeed, many researchers have shown that the complete similarity in the form of a logarithmic law becomes evident only for Karman number $\delta^+ > 5000$. The present data at high Reynolds number seem to disregard this observation.

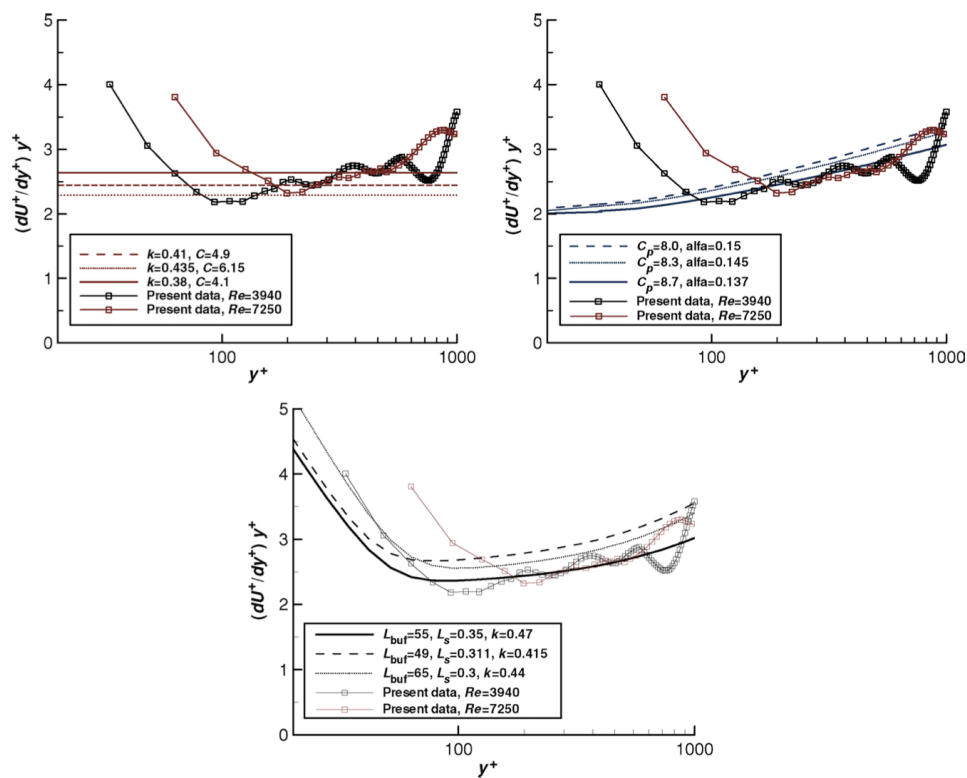


Figure 8 Profiles of $y^+(\partial U^+/\partial y^+) y^+$ from the present data ($Re_\theta = 3940$ and $Re_\theta = 7250$) compared with parametric changes in the logarithmic law of the wall (at the top on the left), parametric changes in the power law of the wall (at the top on the right) and parametric changes in the LOP model (at the bottom).

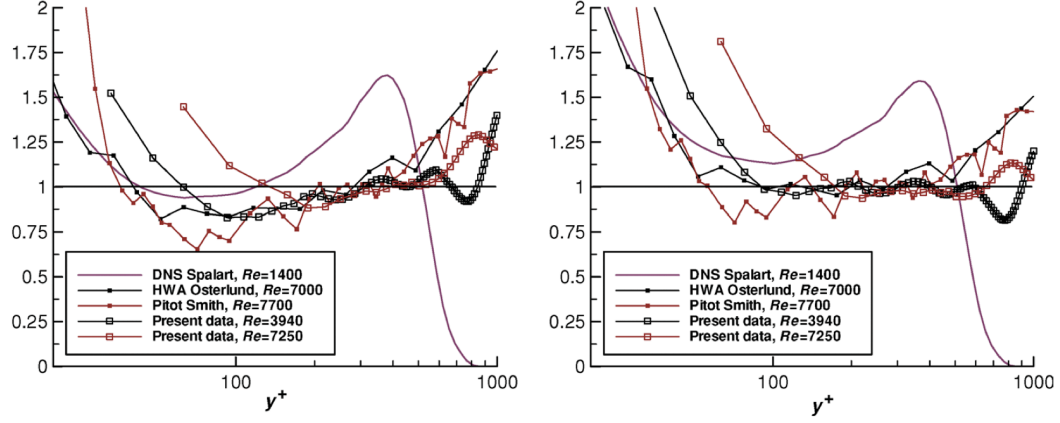


Figure 9 Logarithmic (on the left) and power law (on the right) scaling of profiles of non-dimensional streamwise velocity. Comparison of the present data ($Re_\theta = 3940$ and $Re_\theta = 7250$) with the DNS results by Spalart (1988) and the experimental data by Osterlund et al. (2000) and Smith (1994).

A point to be further investigated is the dependence of the presented models on parameter variations (the ‘constants’ reported at the end of previous section) and if this dependence would strongly change the previous statements. Therefore, in Figure 8 the logarithmic law (plot at the top left), the power law (at the top right) and the LPO model (at the bottom) are presented for some variation of the parameters.

In this representation, the logarithmic law appears as a constant equal to $1/k$ (of course the value of C has no influence), which can account only for the asymptote of the data sets (i.e. for the different Reynolds numbers, as reported by many authors). For the power law (plot at the top right), among the two parameters C_p and α , only the latter is effectively important by influencing the slope of the curve. In comparison to the present data, the best-fit values are $C_p = 8.7$ and $\alpha = 0.137$. Lastly, by a suitable choice of the LPO model parameters it seems possible to account for the whole data set behaviour even in the TBL case (as in the

channel LPO 2008). The best fit values of the three parameters (refer to LPO 2008 for details) are $l_{+buf} = 55$, $l_s = 0.35$ and $k = 0.47$ which are quite different from the optimal values for the channel flow ($l_{+buf} = 49$, $l_s = 0.311$ and $k=0.415$). The last plot concerning the streamwise velocity profile is obtained by plotting in Figure 9 the following quantities (respectively on the left and on the right) as in Zanoun et al. 2003:

$$\frac{dU^+}{dy^+}ky^+, \frac{dU^+}{dy^+} \frac{1}{C_p\alpha} \frac{1}{y^{+(\alpha-1)}}.$$

The former is equal to 1 if the logarithmic law holds, whereas the second is equal to 1 if the power law is verified. From the comparisons presented in Figure 9 on the left, neither the DNS nor the experimental data show constant unitary values within the observed y^+ range. Thus a logarithmic region is not strictly present at the tested Reynolds numbers. On the other hand, in the right figure, there is a clear range ($100 < y^+ < 600$, also depending on the Reynolds number) in which all data (except the DNS probably due to the limited Reynolds number) are more or less constant. This confirms that the present data show power law behaviours but of course does not rule out the LPO model. It is also possible, that the different laws are valid in different regions of the layer. In particular, it seems that some proximity to the logarithmic law is observed for the present data in the region $200 < y^+ < 400$.

In order to improve the description of the statistical properties of the TBL, second-order moments have been also studied for the streamwise and wall-

normal velocity components. The present data have been compared with the DNS and HWA data (Morrison et al. 2004 for pipe and Smith et al. 1994 for TBL) in Figures 10 (mean square values, diagonal components) and 11 (Reynolds stress off-diagonal component). The behaviour of the streamwise mean square value for $y^+ > 50$ is strongly dependent on the Reynolds number.

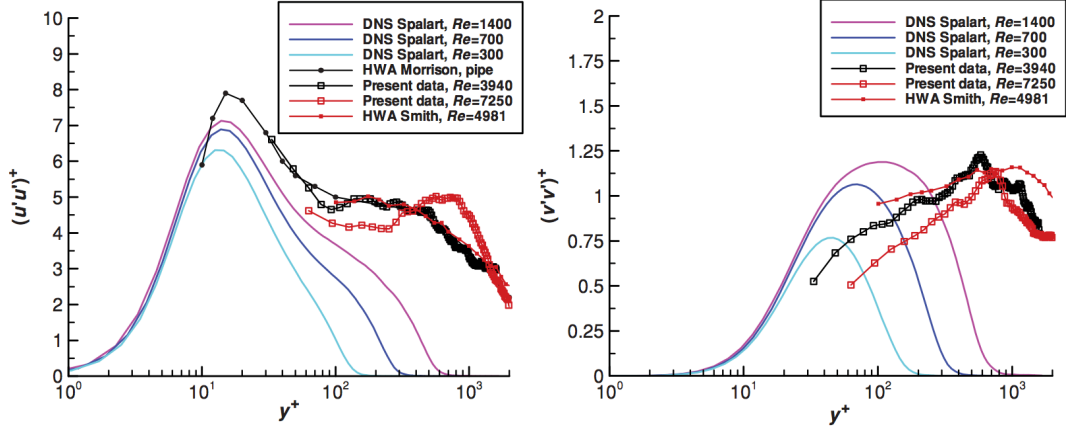


Figure 10 Profiles of non-dimensional rms velocities from the present data (Re_θ 7250) (on the left for u-component and on the right for v-component respectively). Data are compared with the DNS data by Spalart 1988 (at three different Reynolds numbers) and with the experimental data by Morrison et al. 2004 and Smith 1994.

The data and the Reynolds number dependence are in agreement with detailed findings reported in De Graaf et al. 2000 for Reynolds numbers, Re_θ , between 1430 and 31000. In particular, the curve flattens more and more as observed in Morrison et al. 2004, suggesting an increasing turbulent activity in the outer layer. The present data well compare with the HWA data both for the TBL and the pipe flow (thus indicating some similarity between the two). Also the behaviour of the wall-normal component is dependent on Reynolds number and well agrees with the HWA data, exhibiting a far-wall shifting of the maximum

activity and a reduced contribution in the very near-wall region as also reported in De Graaf et al. 2000. The far-wall shift and near-wall reduced contribution are also noticed in Figure 11 in which the Reynolds stress profile is shown. These findings seem to confirm the so-called inactive motion, which is due to large eddies coming from the outer layer influencing the wall motion by increasing the wall-parallel (streamwise and spanwise, the latter not detectable by two-dimensional PIV measurements) velocity components in respect to the wall-normal one.

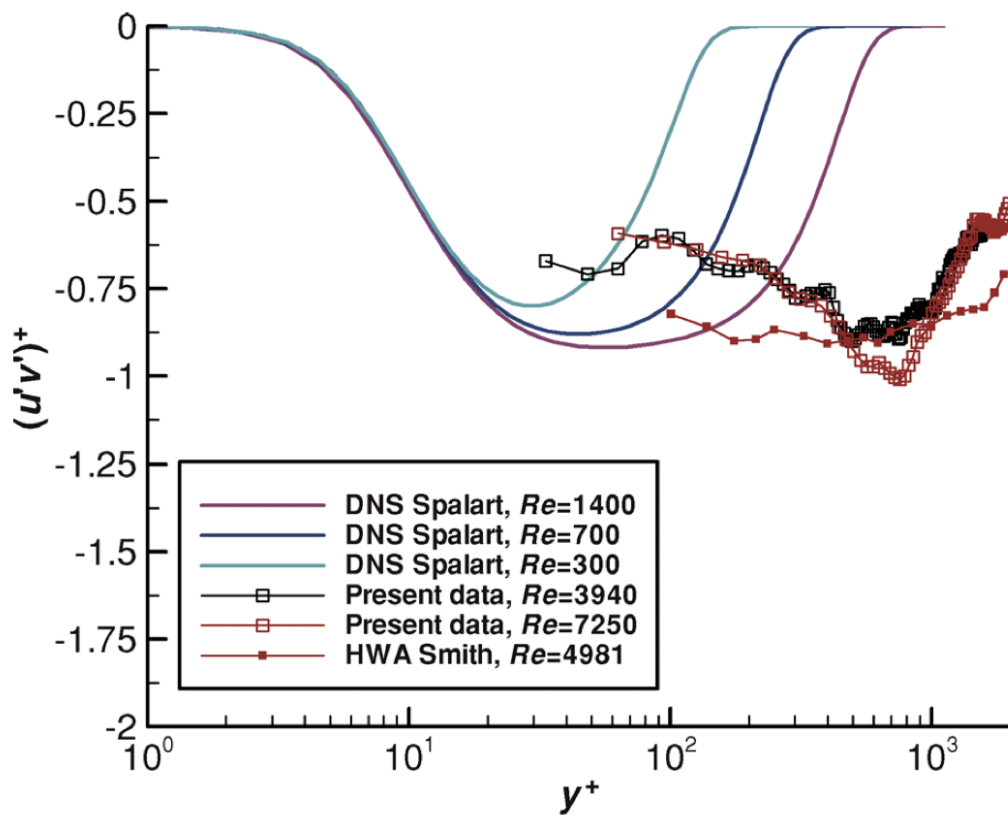


Figure 11 Profiles of non-dimensional Reynolds stress from the present data ($Re_0= 3940$ and $Re_0= 7250$). Data are compared with the DNS data by Spalart (at three different Reynolds numbers) (1988) and with the experimental data by Smith (1994).

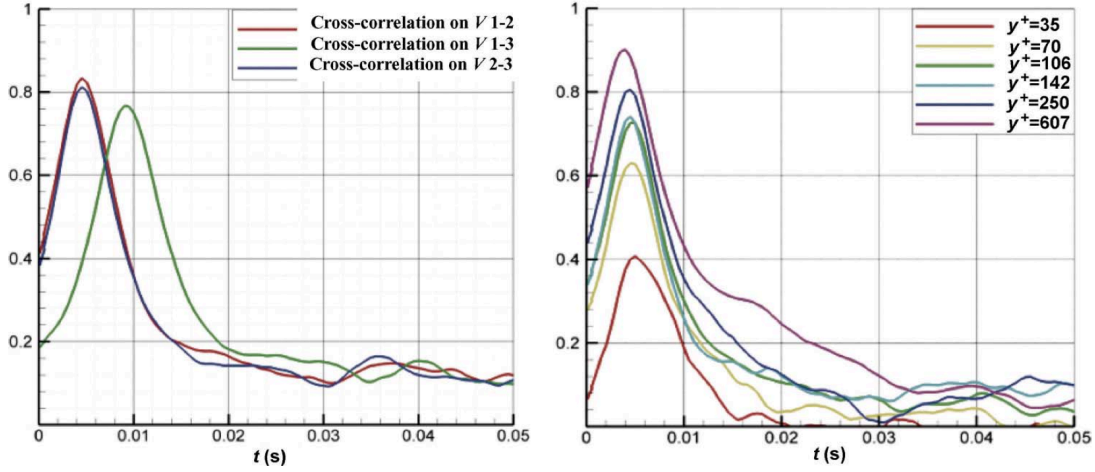


Figure 12 Cross-correlation coefficients of vertical velocity between points separated along the streamwise direction at $y^+ = 250$ (on the left) and overlapping of cross-correlation functions at different distances from the wall (on the right). Data at large Reynolds number, $Re_\theta = 7250$.

4.1.2 Results and comparisons on vortical structures

The average spatial-temporal relations between different points at near-wall locations were investigated by considering cross-correlation time coefficients of velocity components between points along the streamwise direction. In Figure 12, examples of such coefficients are given for the wall-normal velocity component at the largest Reynolds number. As expected these functions exhibit maxima at time separations almost equal to the streamwise distance between points (multiples of 4 mm) divided by the convection velocity (about 1 m/s), i.e. at about 0.004 s and 0.008 s (namely these maxima are just used to evaluate the convection velocity at different distances from the wall). For increasing separation, the value of the maximum decreases (in the left part of the figure) as also when moving closer to the wall (in the right part). In particular, the decrease of correlation at near-wall locations witnesses the increase of vortical structure

activity in such a region. These results are in agreement with previous works on the evaluation of correlation functions in a TBL (Romano et al. 1995).

The attention is then focussed on to instantaneous velocity fields in order to educe near-wall vortices. The investigation is restricted to the region between $y^+ \approx 70$ and $y^+ \approx 250$ in which near-wall structure dynamics takes place. In Figures 13 and 14, examples of sequences of six instantaneous fields are presented for the low Reynolds number (Figure 13) and the large one (Figure 14). In each figure, the Reynolds decomposed vector field (fluctuating part) is shown, whereas plots of the invariant of velocity gradient tensor (Jeong et al. 1995) and of the vorticity field are presented respectively at the top and at the bottom of each instantaneous field. In almost all plots it is possible to observe a good agreement

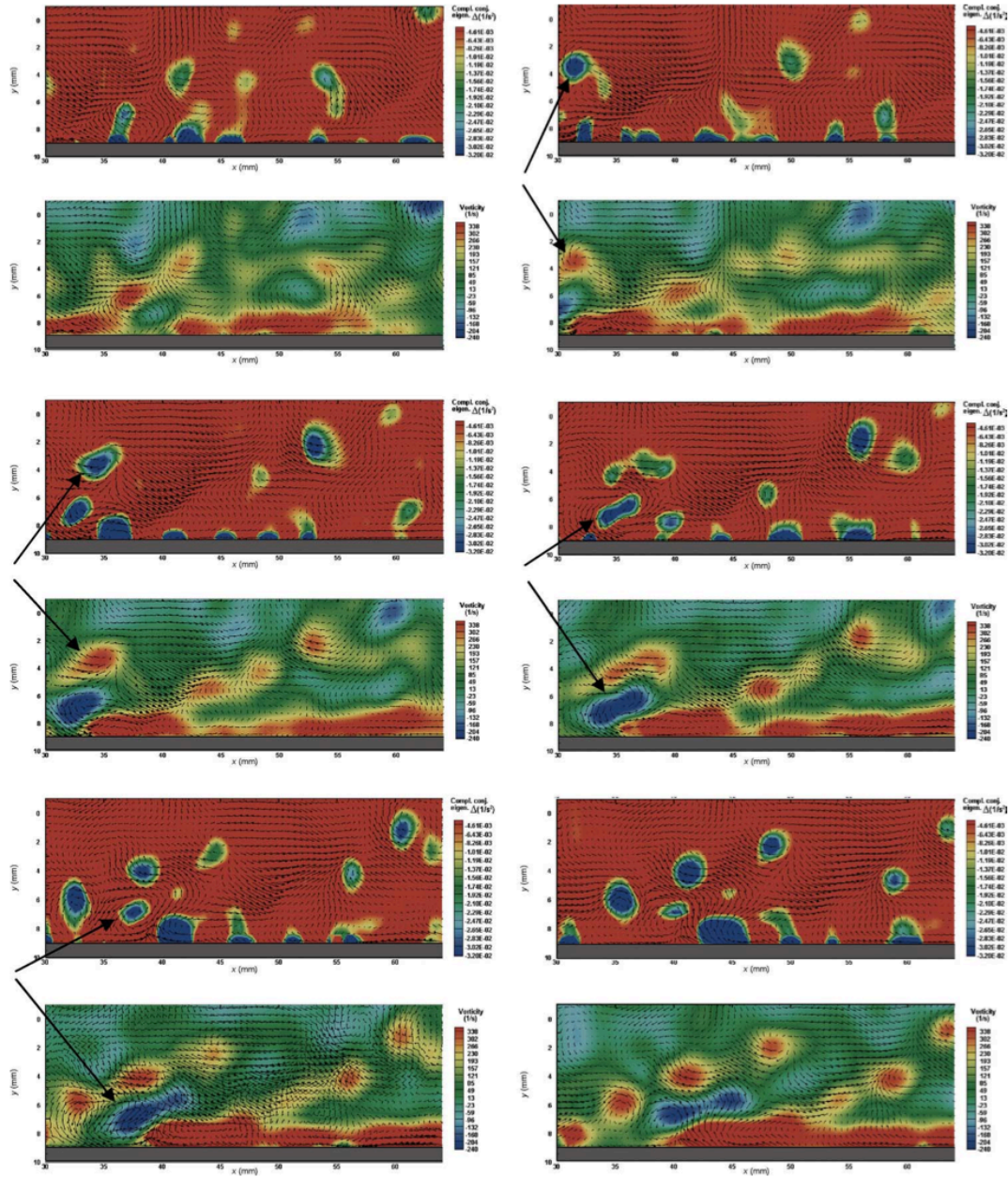


Figure 13 Sequence of six snapshots of instantaneous Reynolds decomposed vector fields separated by $\Delta t = 21 \text{ ms}$ ($\Delta t^+ = 8.4$). At each instant, the colour map shows vortex identification by the criterion of velocity gradient tensor invariant (at the top) and by vorticity (at the bottom). Data at small Reynolds number ($Re_0 = 3940$). The wall is at the bottom.

between the information derived from fluctuating vectors, vorticity and velocity gradient invariant fields, except for the very near-wall region in which velocity

derivatives enhance vorticity contributions and gradient noise (not effectively related to vortices).

Looking at the first sequence presented in Figure 13, it is possible to notice the evolution of a hairpin-shaped vortex linked to a bursting event (indicted by arrows in the second and third plots of the sequence), being stretched by the bottom-up positive wall-normal velocity component, that forces the vortex 'head' to move far from the wall, carrying its 'legs' with it (fourth plot). Then, a counter-rotating vortex very close to the wall stimulates the generation of a new structure similar to the first one, following the same direction. This sequence generates parallel streaks of vorticity production which form with the wall an angle equal to about 30° (arrows in the fourth and fifth plots). Finally, the latter 'breaks' into a 'packet' of vortices aligned to the same direction (sixth plot).

This process is in agreement with the auto-generation and self-sustaining model proposed in Adrian et al. 2000 and Tomkins et al. 2000, in which hairpins are part of a complex pattern (packet) of dynamically linked sub-structures all with more or less the same angular inclination to the wall and the same travelling speed. They are expected to populate a significant fraction of the boundary layer, even at high Reynolds numbers. From present data, several events similar to those shown in Figure 13 can be recognized, thus confirming the packet organization even if the previous 'significant fraction' requires a quantitative determination. As a matter of fact, vortex packets are generated continuously but with some quiescent time interval between one packet and the following one.

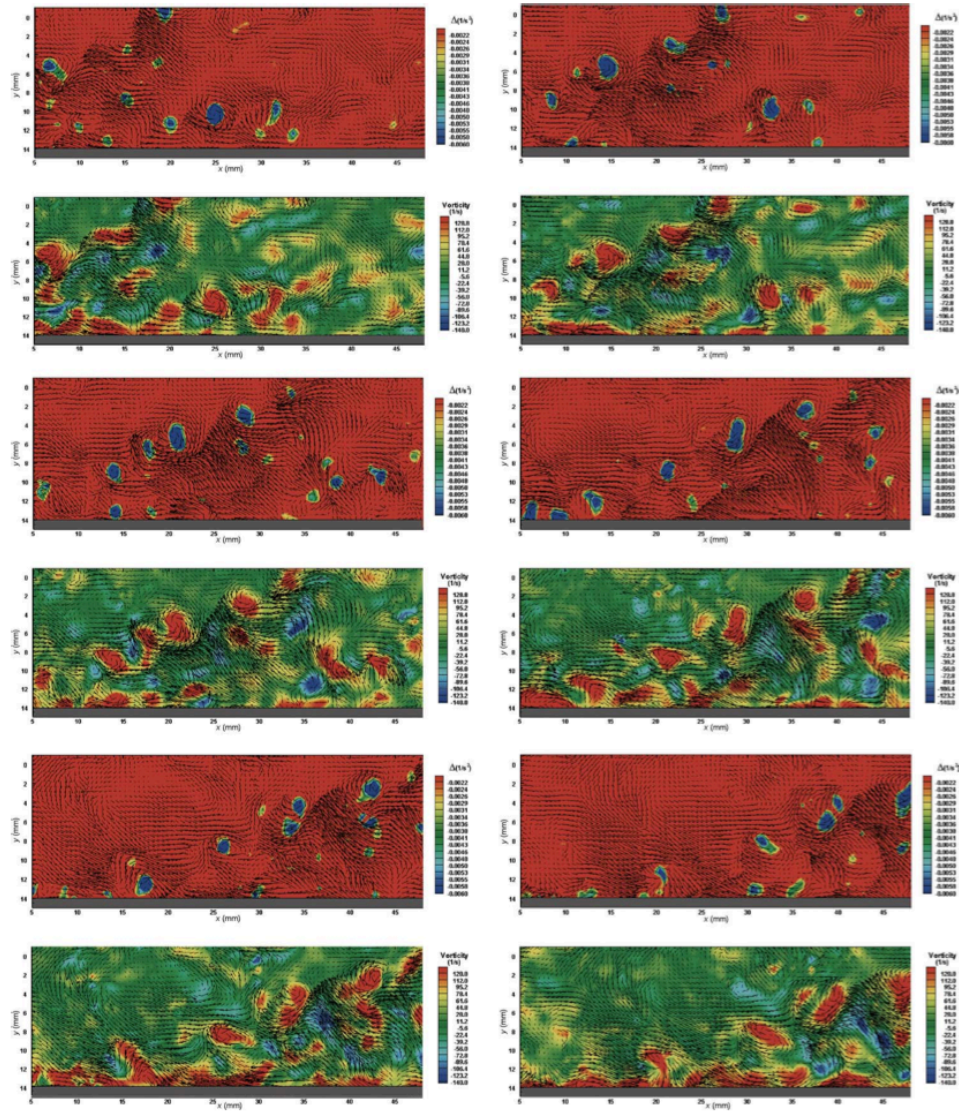


Figure 5 Sequence of six snapshots of instantaneous Reynolds decomposed vector fields separated by $\Delta t = 18$ ms ($\Delta t^+ = 28.8$). At each instant, the colour map shows vortex identification by the criterion of velocity gradient tensor invariant (at the top) and by vorticity (at the bottom). Data at large Reynolds number ($Re_\theta = 7250$). The wall is at the bottom.

The second sequence is presented in Figure 14 and refers to the largest Reynolds number ($Re_\theta = 7250$). Even at such a high Reynolds number the previous vortex dynamics is detectable, although the average size of the educed vortices is smaller than before and the velocity gradients are higher. (Eduction derived

from the velocity gradient tensor seems now to be more effective than from vorticity.) Also in these conditions vortex structure packets are observed as sequences of inclined (about 30°) minima of the invariant of velocity gradient tensor (Jeong et al. 1995) and alternating maxima–minima of vorticity.

Lastly, the investigation is focussed on to the evaluation of the effective contribution of such packet events to the entire spectrum of wall dynamics events. In some sense, the following is a possible evaluation of the importance of coherent over non-coherent events in the TBL. The investigation of this aspect is suggested not only from the previous evidence of quiescent periods at all Reynolds numbers but also from the fact that at the largest Reynolds number the presence of vortex packets seems to be different than at the smaller value. Thus, a statistical evaluation of deduced vortex presence in the TBL is performed by using the wavelet tool.

Statistical approaches on the streak appearance in buffer-layer TBL dynamics have very recently received considerable attention (Lin et al. 2008). It is well known that the wavelet analysis gives information not only about vortex position but about their size too. The algorithm used in the present work is based on the complex continuous wavelet transform (Farge et al. 1992). The adopted wavelet has been the Mexican hat to evaluate the local energy distribution, while structure identification has been performed by the LIM (Farge et al. 1992).. The connection between LIM peaks and vortices in a PIV field has already been shown (Camussi et al. 2002). In the present work, the two-dimensional PIV vector fields are considered as one-dimensional slices at the different scales.

Thus, the wavelet transform of the field is performed row by row in the streamwise direction on the wall-normal velocity component.

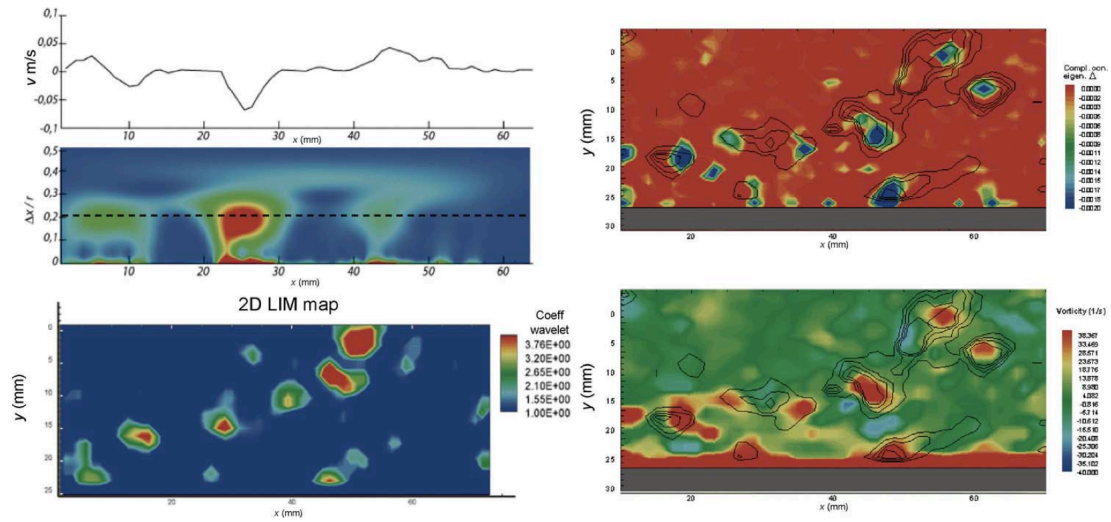


Figure 6 Example of LIM obtained by wavelets with one-dimensional slice (at the top left) and global map (at the bottom left) and comparison between wavelet (contours on the right figures), velocity gradient invariant (at the top right) and vorticity (at the bottom right) criteria. Data at small Reynolds number ($Re_0 = 3940$). The wall is at the bottom.

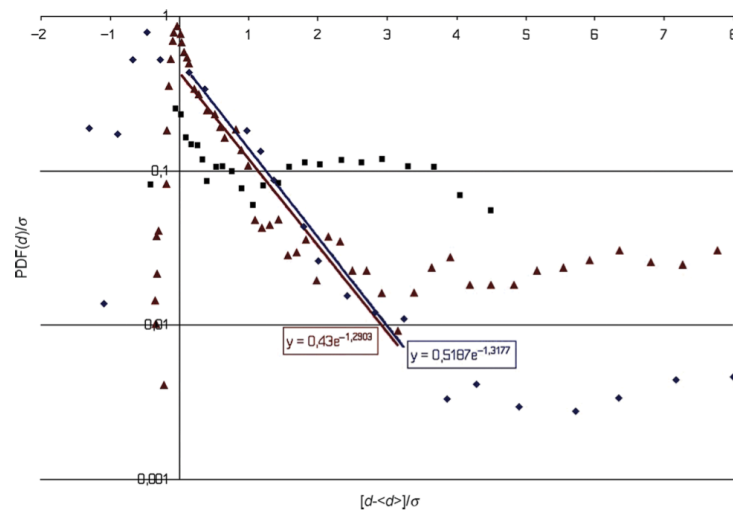


Figure 16 Probability density distribution of vortex size obtained by wavelet analysis (semi-log plot). Data at small ($Re_0 = 3940$, blue diamond) and larger Reynolds number ($Re_0 = 7250$, red triangles). Data from a purely noise field are indicated by black rectangles. PDF denotes probability density function.

An LIM map is plotted with respect to the streamwise direction x and investigated scale r . For each scale (i.e. each row), the peak LIM is found and used to evaluate the vortex position, whereas the size is derived from the amplitude of the LIM peak.

The global LIM map is finally determined by combining all scales. In the left part of Figure 15, this process is exemplified for one instantaneous image at the lowest Reynolds number. In the right part of the figure, the comparison between LIM maxima, velocity gradient tensor invariant and vorticity is shown. The agreement between the various vortex eduction methods is noticeable except for the very near-wall region when considering vorticity.

So far, to attain information on the wall structure dynamics, the probability density function of identified vortex size is computed. The result is shown in Figure 16 together with the results obtained from a pure incoherent noisy vector field generated artificially. (The horizontal axis represents the vortex diameter scaled by its average and rms value.) The present results obtained for

$50 < y^+ < 300$ are in agreement with those obtained in Camussi et al. 2002 at different Reynolds numbers: the TBL is characterized by a strongly non-symmetric size distribution around the mean (the mean size is equal to about 0.1δ). The vortices larger than the average have a distribution which shows less and less importance following an exponential decay for increasing vortex size. This decay is definitely different from the distribution obtained in the case of incoherent noisy images in which a constant value is attained. The exponential decay indicates some existing hierarchical relation among different vortex scales which could be in agreement with regeneration near-wall models. To this end, it

is important to remark that the observed distribution is definitely not a Poisson distribution (which is related to rare uncorrelated events, thus discharging any relation among structures); rather it is quite close to a Gumbel distribution (Dean et al. 2001) which is derived from statistical independent events but still related hierarchically in a cascade. This could mean that when a ‘parent’ vortex is formed (size almost equal to the average) it generates a cascade of ‘children’ vortices. The values determined for the exponential law (best fit $0.5 \times e^{-1.3(d-\bar{d})/\sigma_d}$, almost independent on Reynolds number) indicates that for each ‘parent’, with size d , there are about seven ‘children’ having a size equal to $d-\sigma_d$. On the other hand, there is not any hierarchy for vortices smaller than the average.

It seems that the present analysis points out a quite large relevance of ‘coherent’ packets of vortical structures due to the fact that the probability of ‘non-coherent’ part for the present data is almost 10 times lower than that obtained from pure noisy vector fields (the flat parts in Figure 16). The described behaviours seem to be almost the same at the two different Reynolds numbers, thus indicating that the wall dynamics is substantially the same (of course when scaled to the average vortex size).

4.2 Forward Facing Step (FFS)

4.2.1 The recirculation region

The averaged PIV fields have been analysed to identify the main flow features, determine the properties of the recirculation bubbles and evaluate the effect of Re_h upon the overall flow physics. Examples of averaged vorticity fields, with the

corresponding streamlines are reported in Fig. 17 for two different Re_h in the region upstream of the step.

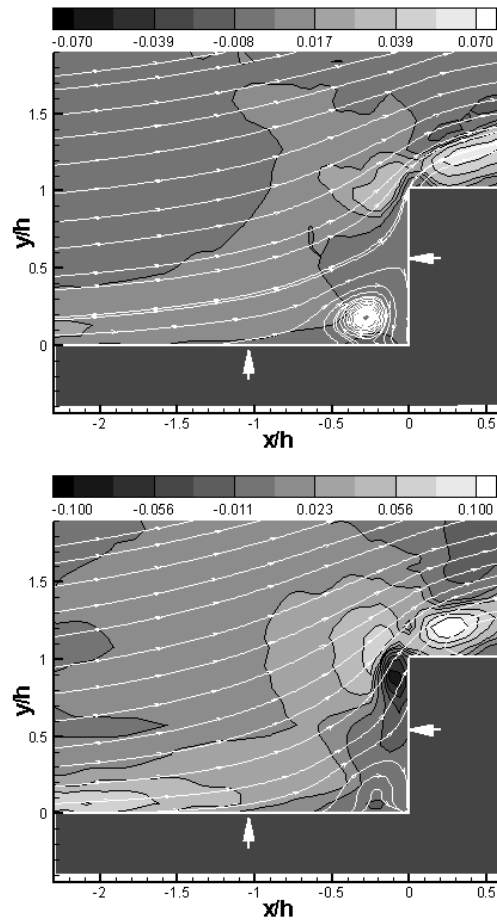


Figure 7 Averaged vorticity field (contour) and streamlines (white lines) obtained at $Re_h=8800$ (top plot) and $Re_h=26300$ (bottom plot). The white arrows indicate the separation point upstream of the step (at $x / h \sim -1$) and the reattachment position on the vertical side of the step front (at $y/h \sim 0.5$).

It is shown that, according to results reported in Leclercq et al. 1999, the separation occurs independently of Re_h at about one step's height upstream of the discontinuity while the reattachment occurs at about half the vertical step's height.

Instead, the extension of the recirculation region downstream of the step seems to depend upon Re_h in a more relevant manner. Examples are reported in Figure

18 showing that the average location of the reattachment point moves from about $1.5h$ downstream of the step at the lowest Re_h up to about $2.1h$ for the highest case. These observations are in reasonable agreement with the results reported in Leclercq et al. 2001 and Farabee et al. 1986.

In Figure 19, we show the complete mean velocity field for the lowest Re_h , where the two separate PIV measurements have been patched together. We also report a series of wall profiles of the velocity longitudinal component, extracted from the PIV dataset.

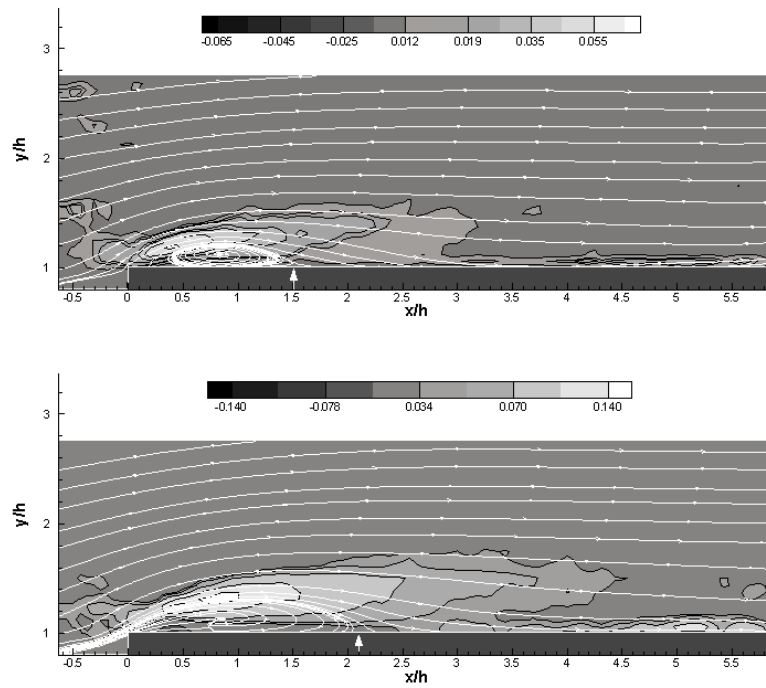


Figure 8 Same as the previous plot but in the downstream region. The white arrows indicate the approximate position of the reattachment point.

The normalized axial velocity profiles have been compared with LES simulations found in the literature (see figure 20). Although these numerical simulations have been done for a much higher Re_h (1.7×10^5), we chose to perform the comparison with the experimental data obtained at the lowest $Re_h = 4400$ to

demonstrate that there is indeed a good agreement across the full range of Re_h considered here. In fact, a very good agreement is seen upstream of the step whereas larger discrepancies are found downstream. This result seems to confirm that the flow properties in the region upstream of the step are less dependent upon the governing parameters with respect to those in the region downstream of the geometrical discontinuity.

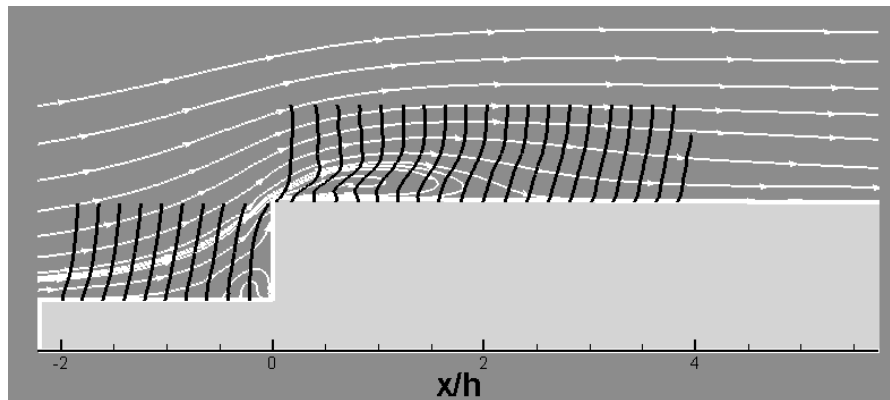


Figure 9 Full field plot of the mean velocity field obtained at $Re_h=8800$. Longitudinal velocity profiles extracted from the PIV analysis are also plotted at several locations upstream and downstream of the step.

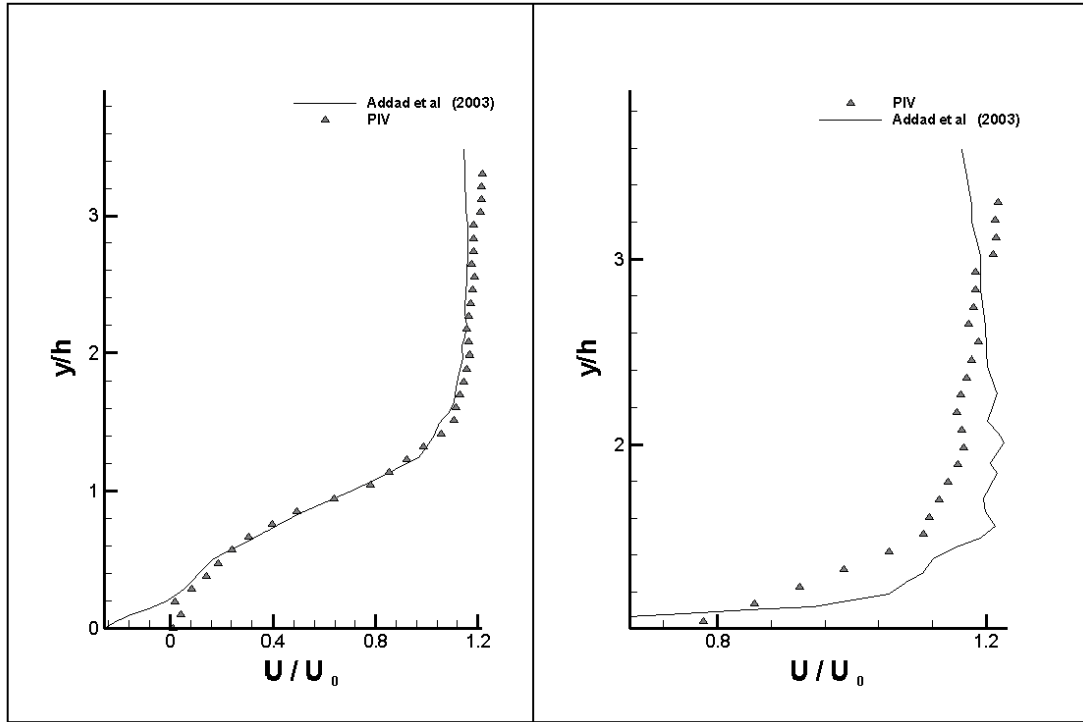


Figure 10 Velocity profiles extracted from the PIV data at $Re_h=8800$ compared with results reported in Song et al. 2000. The left plot corresponds to a position just upstream of the step ($x/h=-0.3$); the right plot corresponds to a position immediately downstream of the step ($x/h=0.5$).

4.2.2 Wall Pressure Statistics

The statistics of the pressure fluctuations have been established through the computation of the root mean square pressure coefficient Cp_{rms} , defined as

$$Cp_{rms} = \frac{\sigma_p}{\frac{1}{2}\rho U_0^2}$$

where σ_p represents the standard deviation of the pressure and ρ is the fluid density. The evolution of $C_{p_{rms}}$ as a function of both the non-dimensional distance to the step and Re_h is reported in Fig. 21.

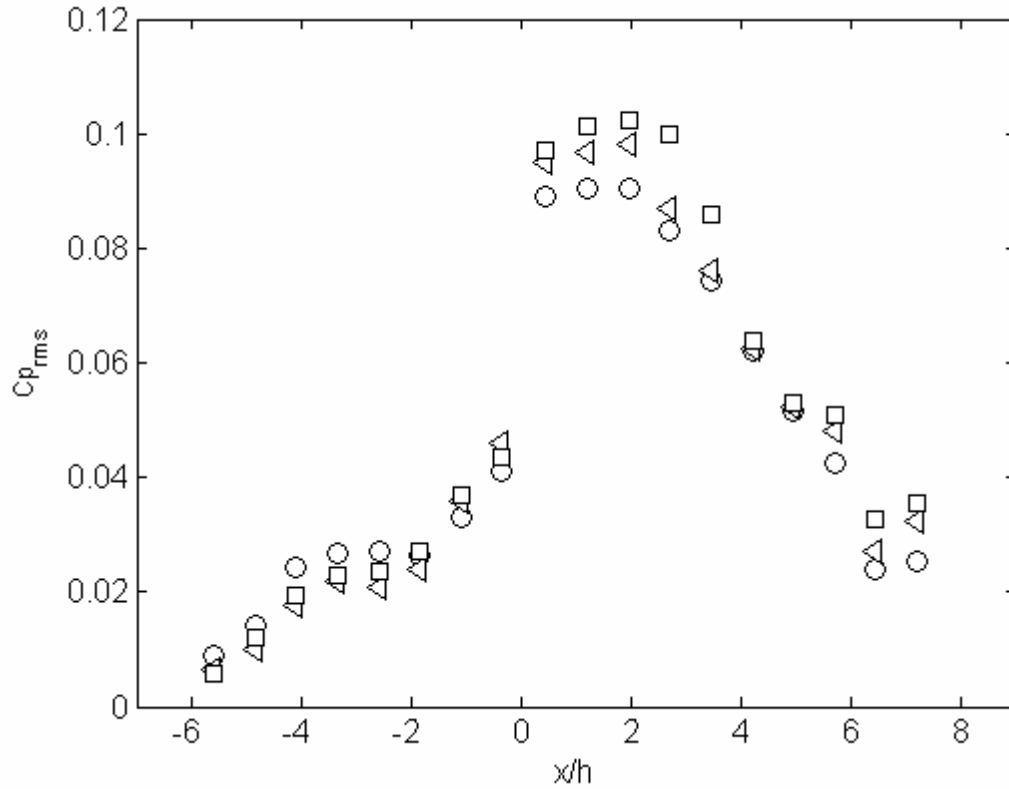


Figure 11 Evolution of the $C_{p_{rms}}$ in terms of the distance from the step and for different free stream velocities. Circles correspond to $U_0 = 0.5$ m / s, triangles to $U_0 = 1$ m/s, and squares to $U_0 = 1.5$ m/s.

In the region upstream of the step, it is clearly shown that the largest pressure levels are reached close to the location of the vertical side and a satisfactory collapse of the results is obtained for different velocities. Downstream of the step up to about $x/h = 3.5$, we observe a larger dispersion that is associated to the varying dimensions of the recirculation region, which are affected by Re_h . A similar result was obtained, for instance, by Hudy et al. and Cherry et al. The analysis of the instantaneous velocity fields provided by the time-resolved PIV measurements confirms that the position of the flow reattachment is strongly

time-dependent. The maximum amplitude of the Cp_{rms} coefficient is found to correspond approximately to the location of the mean reattachment point of the recirculation bubble.

Regarding the overall evolution of Cp_{rms} , it is noticeable that the largest wall pressure fluctuations occur in the region immediately downstream of the step. Hence from a hydrodynamic viewpoint, the predominant wall pressure source appears to be the recirculation bubble located downstream of the step and, more specifically, the unsteady reattachment point located at about $2-3h$ from the wall discontinuity. Previous studies have established that the upstream region would display the largest fluctuations in terms of acoustic emission. Their authors linked these high fluctuations to the impact of the flow structures over the vertical side of the step. In view of this and of the present results, the downstream region of the FFS is found to be more efficient in terms of wall pressure intensity, whereas the upstream side is more relevant from the acoustic standpoint.

PDFs of the wall pressure fluctuations have been computed at different locations and for the different Re_h . The random variable is represented in its reduced form, i.e. normalized in order to have zero-mean and unitary standard deviation. The results reported in Fig. 22 correspond to the cases obtained upstream of the vertical side of the step. It is clearly shown that the PDF shapes are independent of both the distance to the step and Re_h .

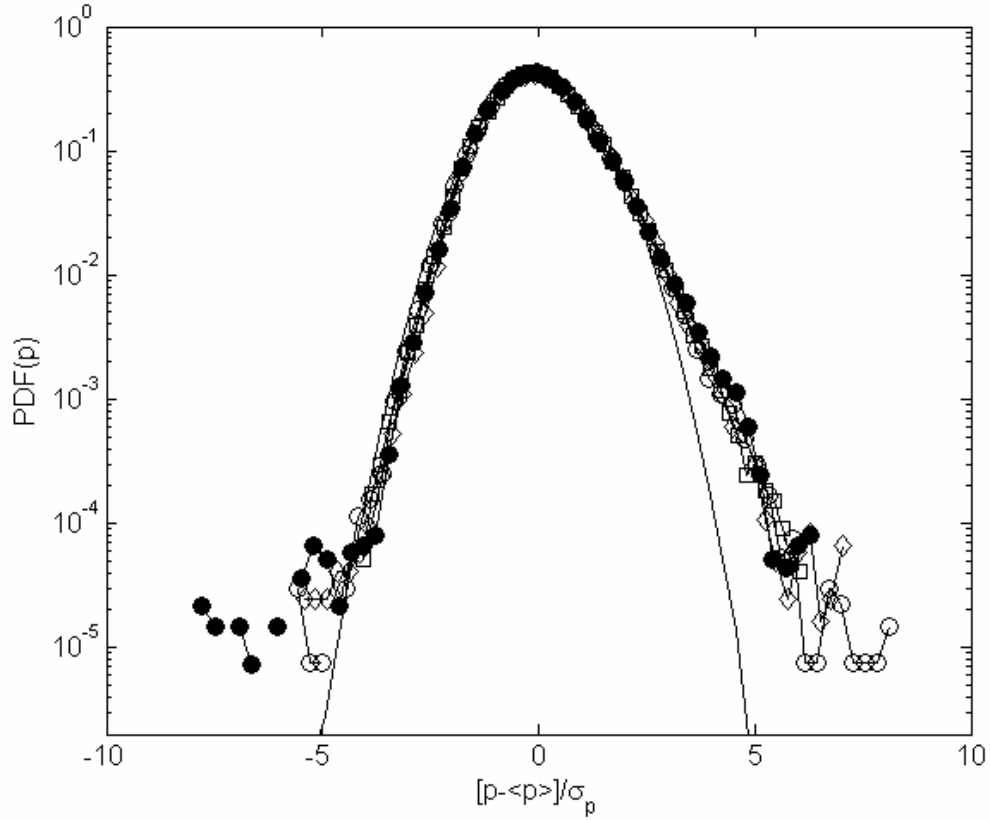


Figure 12 PDF of the wall pressure fluctuations reported in reduced variables. Different symbols correspond to different locations upstream of the step: circles correspond to $x=-4.85h$, squares to $x=-2.6h$, and diamonds to $x=-0.35h$; filled symbols are computed at $Re_h=8800$ and empty symbols are computed at $Re_h= 26300$ (note that at lowest Re_h only one case is reported for clarity). The solid line (no symbols) represents a reference Gaussian curve.

The PDFs are skewed towards positive values and, in every case, a departure from the reference Gaussian curve is visible. The origin of such a behaviour can be ascribed to the effect of pressure surges, which are statistically relevant in the region upstream of the step where a significant pressure gradient is present. In this regard, Kiya & Sasaki observed a positive skewness of the wall-pressure fluctuations in the re-attaching zone of a separated region and interpreted this behaviour as induced by inrush of irrotational flow towards the wall. More

recently, a positive skewness in the pressure fluctuation statistics has been observed in front of forward-facing steps located along the fuselage of an instrumented aircraft.

A somewhat different behaviour is found downstream of the step, see Fig. 23. The results indicate a lack of universality, especially close to the step. Indeed, a collapse of the curves is no longer observed and a major dependency upon both the distance to the step and Re_h is established, in agreement with the overall flow physics described in the previous subsection. It is also confirmed that the wall pressure PDFs are non-Gaussian even though the departure from the reference Gaussian curve occurs both for positive and negative fluctuations.

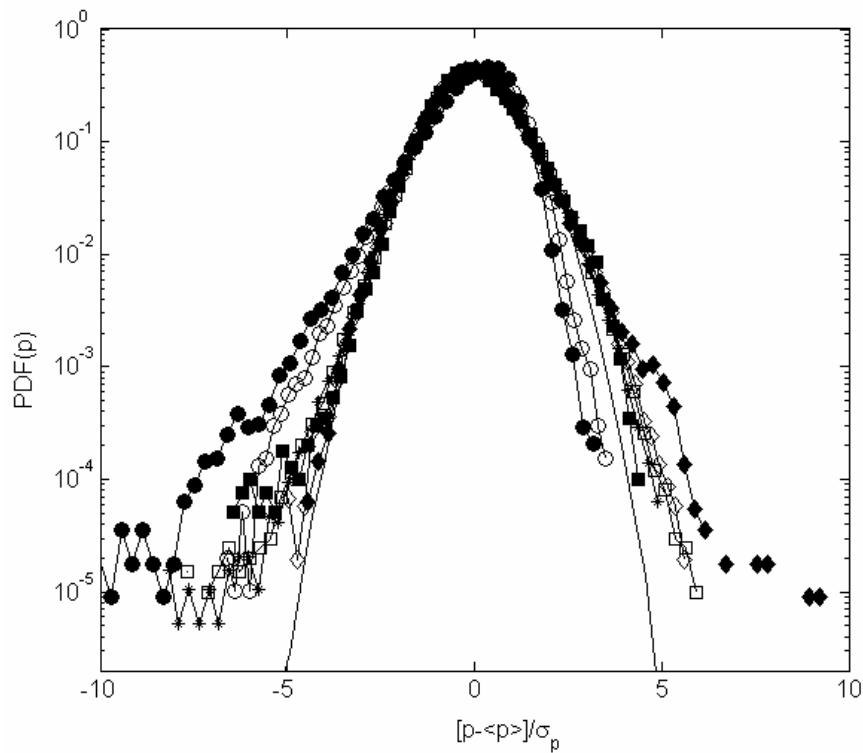


Figure 13 Same as the previous plot but for locations downstream of the step: circles correspond to $x = 0.45h$, squares correspond to $x = 1.95h$, and diamonds correspond to $x = 2.7h$; filled symbols are computed at $Re_h = 8800$ and empty symbols are computed at $Re_h = 26300$ (note that all the cases at the lowest Re_h are reported).

The statistical analysis is further extended through the computation of the Fourier spectra. The wall pressure spectra presented hereafter have been decontaminated from the background noise measured with the inflow hydrophones using the procedure presented in Carley et al. 2000 and successfully applied to the case of wall pressure fluctuations. The procedure is based on the computation of the coherence function between the wall pressure signal $p(t)$ and a reference signal representing the background noise $n(t)$. The contribution of the background noise to the overall spectrum is provided by the coherence function between these two signals:

$$\gamma_{np}^2 = \frac{|S_{np}(f)|^2}{S_{nn}(f)S_{pp}(f)}$$

where f represents the frequency, S_{pp} and S_{nn} denote the autospectra of the signal p and the noise n respectively, and S_{np} is their cross-spectrum. The autospectrum cleaned from the background noise is given by the following expression:

$$S_{pp}^t(f) = (1 - \gamma_{np}^2(f))S_{pp}(f)$$

The spectra presented in the following sections are to be understood as the cleaned counterpart of the original spectra. The overall evolution of the frequency spectra measured upstream of the step for the lowest Re_h is presented in Fig. 24.

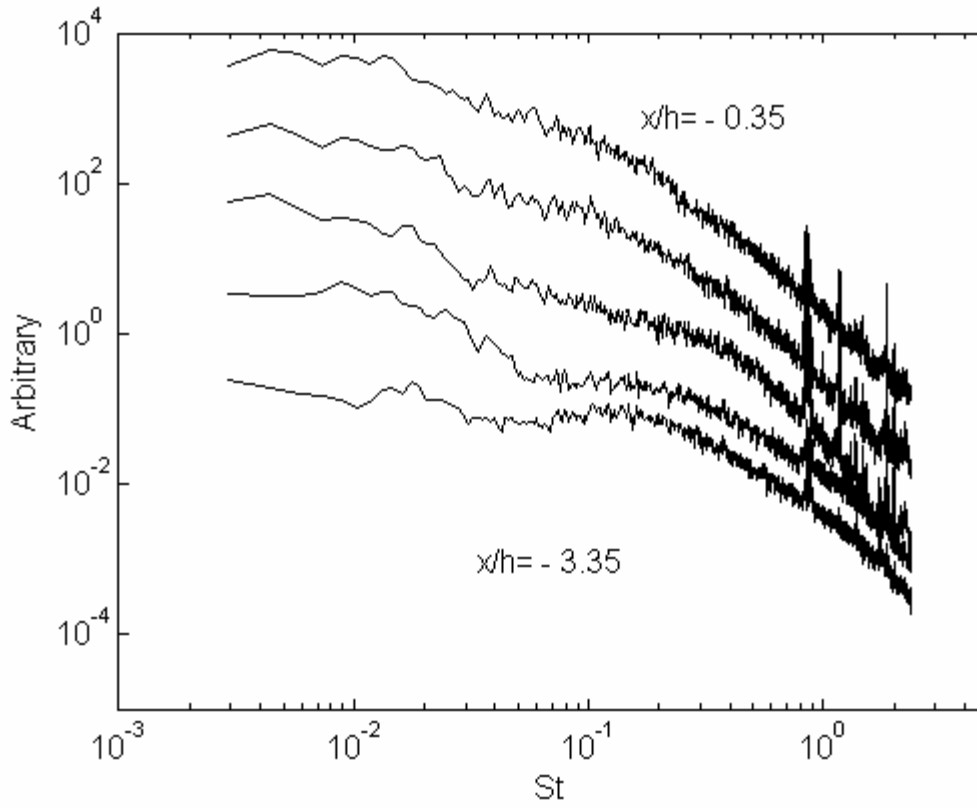


Figure 14 Wall pressure spectra obtained at $Re_h = 8800$ for different positions upstream of the step. For the sake of clarity, the amplitude of each spectrum is arbitrarily shifted along the ordinate and the streamwise direction is from bottom to top. The top spectrum is measured at $x/h = -0.35$ and the bottom spectrum is measured at $x/h = -3.35$. The separation between consecutive spectra is $0.75h$.

The power spectral densities (PSD) computed at different locations are reported versus the non-dimensional frequency St defined on the basis of the free stream velocity and of the step's height. Note that the plots have been shifted along the vertical axis for clarity of display. It is seen that the energy content in the low frequency range increases as one approaches the step, indicating the onset of larger scale dynamics. The variations observed on the decay laws of the different frequency spectra are consistent with this idea. A transition region is found

around $x/h=-1.85$, where the energy transfer is taking place between the smaller scales and the growing larger ones.

This effect is further evidenced in Fig. 25 where the spectra obtained in two positions, very close and far upstream from the step, are reported together in non-dimensional form and for a fixed Re_h . The main contribution to the low frequency energy content can be ascribed to the flapping motion of the recirculation bubble (see e.g. Largeau & Moriniere), which is characterized by a Strouhal number around 0.01, as per e.g. Hudy et al. Similar results, obtained at higher freestream velocities, not reported here for brevity of discussion, point to the fact that this phenomenon is independent of Re_h .

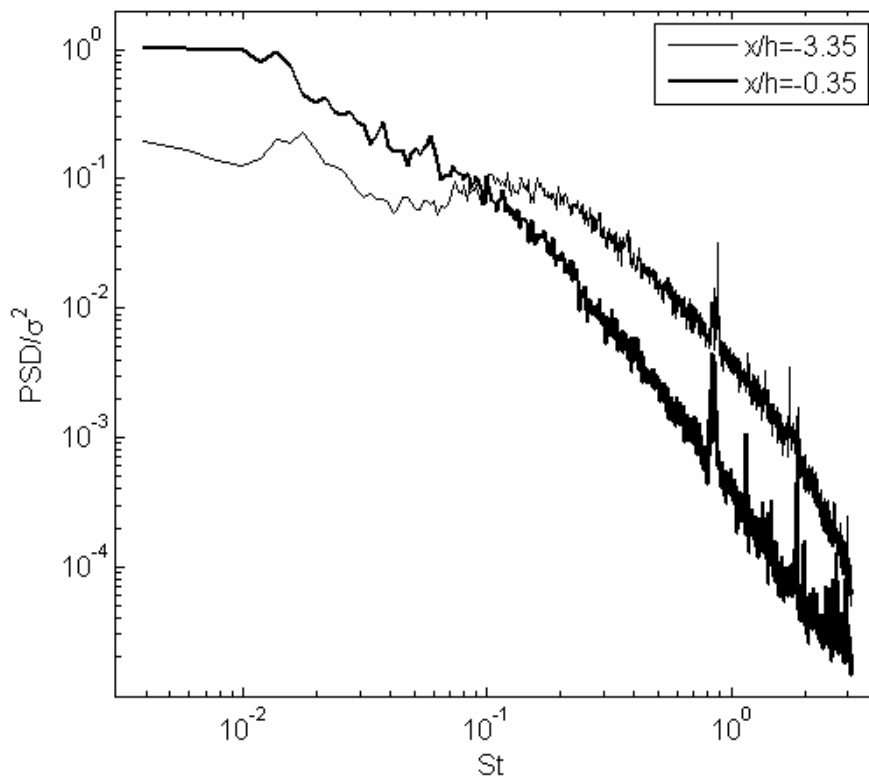


Figure 15 Nondimensional pressure spectra obtained at $Re_h= 8800$ for pressure transducers located inside ($x/h=-0.35$) and outside ($x / h = -3.35$) the recirculation bubble upstream of the step.

The low frequency excitation leads to a broadband effect, which results into a decay law of the pressure spectra significantly different from what is expected in equilibrium turbulent boundary layers. A similarity with equilibrium TBL is only found for locations sufficiently far upstream of the step. In this case, the shape of the wavenumber spectra is directly connected to the vortical structures embedded within the turbulent boundary layer, as suggested by Farabee and Casarella. Specifically, these authors suggested that the contribution to high-wavenumber components can be attributed to fluid dynamic structures in the near wall region, whereas large scale structures in the outer layer influence the low wavenumber domain. Results presented in Bradshaw et al. 1967 and Goody et al. 2000 further suggest that the wall pressure spectra would decay as power laws with an exponent close to -1 due to the effect of the coherent structures present in the outer region of the TBL. As the separation region is approached, a power law decay closer to the exponent -7/3 is usually observed. The $f^{7/3}$ power law is the one expected in homogeneous and isotropic turbulence and it has been found also within regions of separated flow, for instance downstream of rearward steps. Examples of power spectra obtained within the upstream recirculation region are presented in Fig. 26 for three different Re_h . In this case, it is interesting to note that the -1 and the -7/3 scalings coexist. Results obtained at different positions upstream (not shown here) confirm that the -7/3 decay law becomes predominant as the distance to the step decreases.

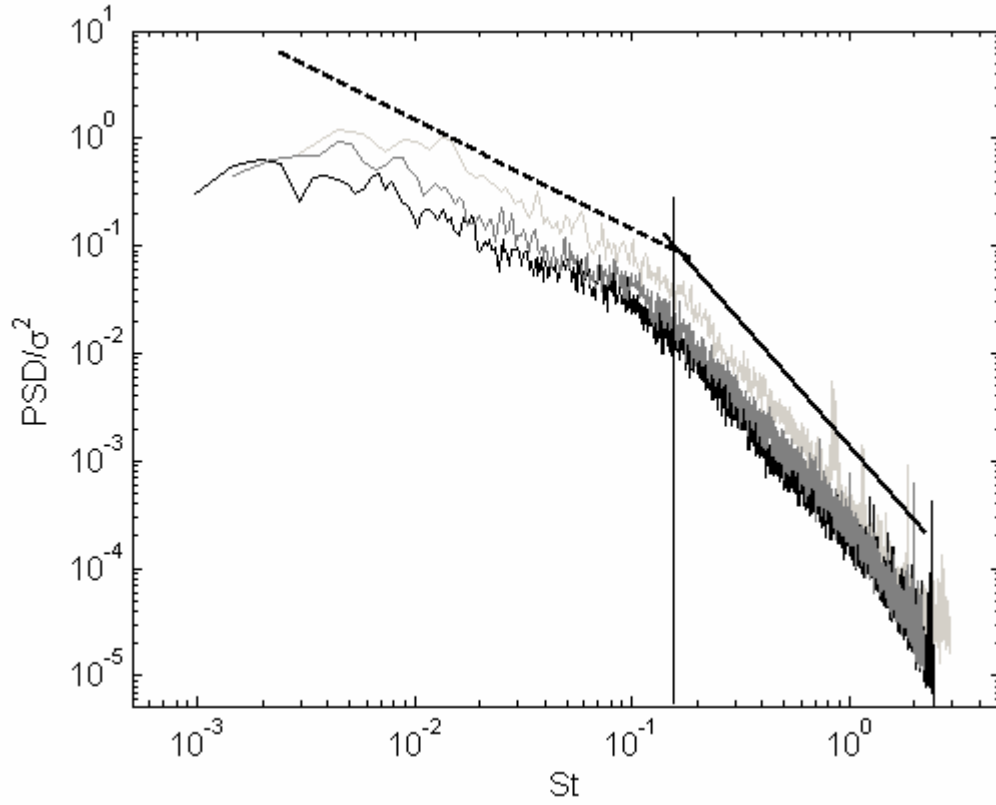


Figure 16 Normalized power spectra obtained at $x/h = -0.35$ for $Re_h = 8800$ (bright gray line), $Re_h = 13200$ (dark gray line), and $Re_h = 26300$ (black line). The dashed straight line denotes the power law with exponent of -1 while the solid straight line represents the $-7/3$ power law. The vertical straight line denotes the approximate position of the crossover Strouhal number between the -1 and the $-7/3$ power laws of the spectra.

It is also observed that such a behaviour is independent of Re_h since the two scalings are equally present for the whole set of velocities. However, the frequency corresponding to the cross-over between the two scaling laws is seen to depend on Re_h since it increases with Re_h thus leading the -1 and the $-7/3$ scaling law regions to extend further towards higher frequencies. The mechanism that links the cross-over frequency and Re_h is driven by a Strouhal law based on the flow upstream velocity and on the step's height. Indeed, when the spectra are plotted against the non-dimensional Strouhal number St (see Fig.

26) it is seen that the transition between the two scalings occurs for a St value fairly constant that is comprised between 0.1 and 0.2, regardless of Re_h . Also, it has been verified that the step's height is the only valid cross-over length scale since other length scales characterizing the flow, such as the incoming boundary layer displacement thickness, did not made the pressure spectra plots to collapse as in fig. 26.

As for the downstream region of the step, the measured wall pressure spectra are again quite different from those commonly obtained in equilibrium boundary layers. The behaviour of the pressure PSD is illustrated in Figs. 27 and 28 for different locations downstream of the step, respectively for the lowest and highest Re_h .

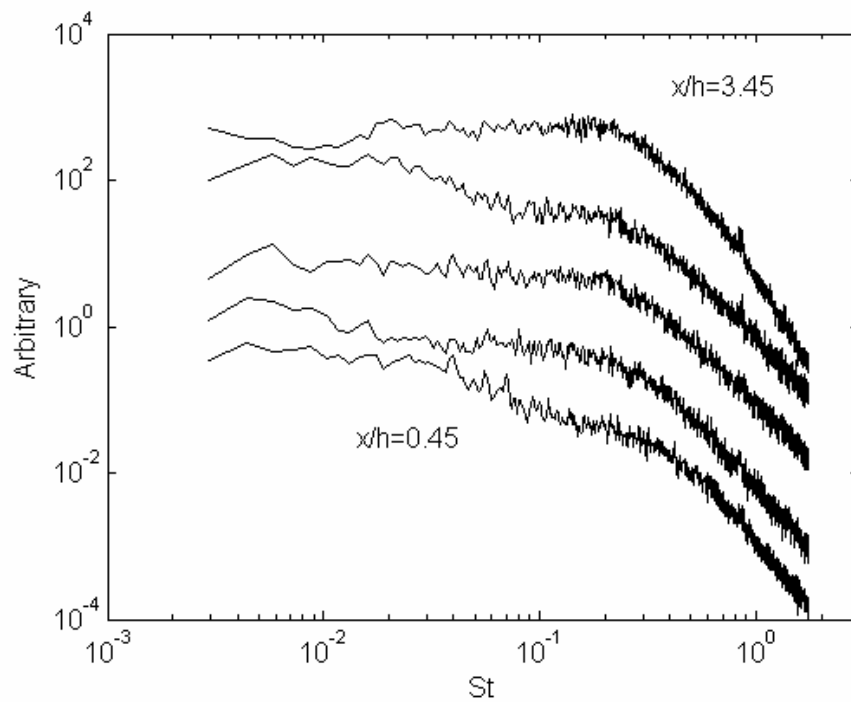


Figure 17 Wall pressure spectra obtained at $Re_h = 8800$ for different positions downstream of the step. The amplitudes of each spectrum are arbitrarily shifted along the ordinate and the streamwise direction is from bottom to top. The top spectrum is measured at $x/h=3.45$, and the bottom spectrum is measured at $x/h=0.45$. The separation between consecutive spectra is $0.75h$.

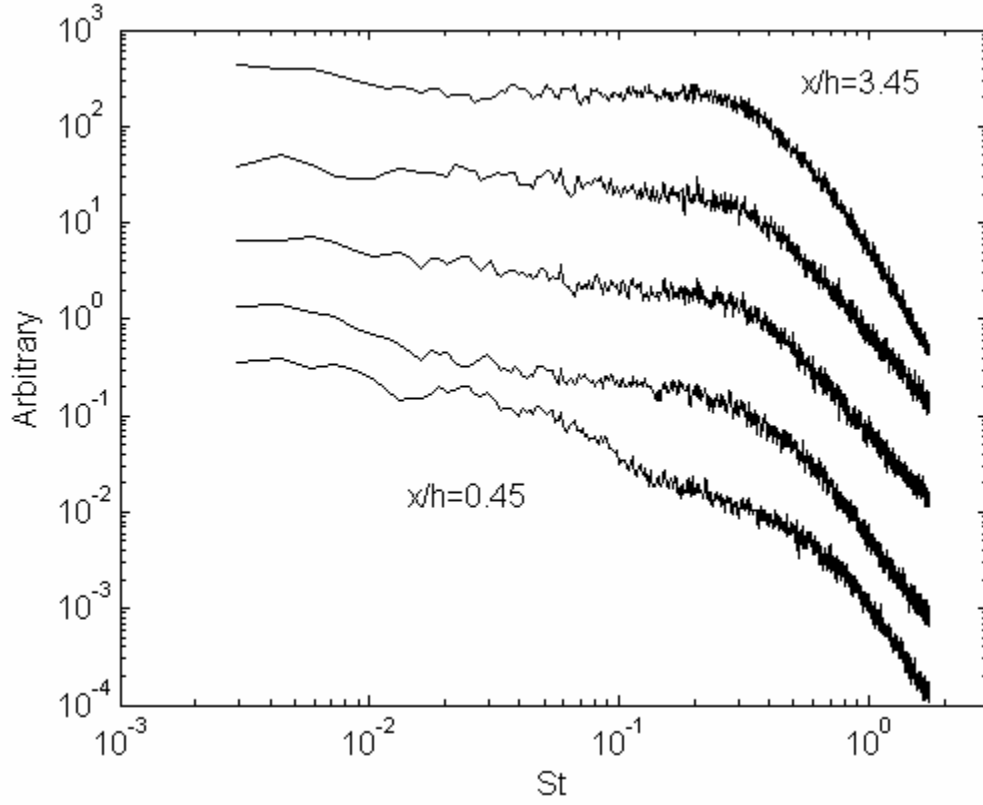


Figure 18 Same as the previous plot but for $Re_h = 26\,300$.

The spectra evolution is similar to that observed in separated flows by Cherry et al. and Hudy et al. Similarly to the upstream case, the evolution of the spectra immediately downstream of the discontinuity points to a large scale mechanism that manifests itself through a low frequency amplification around $St \approx 0.01$. Similar results are reported by Hoarau et al. in the separated region downstream of a forward facing ramp. As we move downstream, the large scale structures found in the shear layer cause the energy content to increase in a narrow band around $St = 0.2$ (see Hudy et al. 2003). This behaviour is better rendered in Fig. 29 where we report the non-normalized spectra obtained at three different locations and for the lowest Re_h .

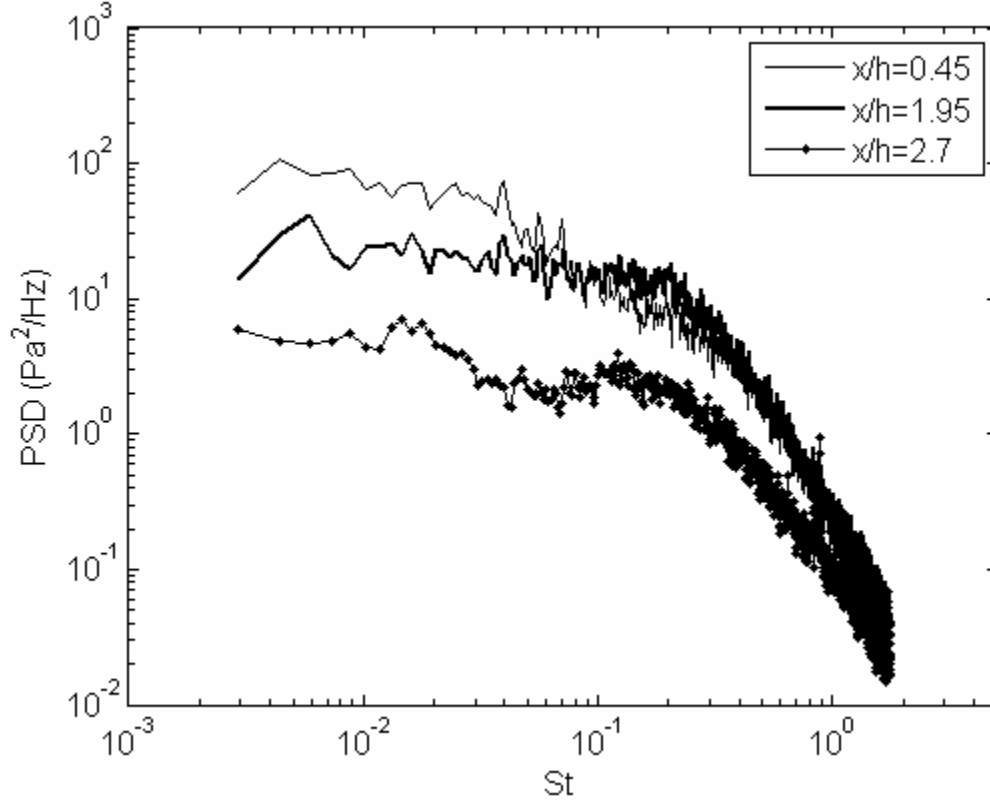


Figure 19 Pressure spectra obtained at $Re_h = 8800$ for pressure transducers located close to the recirculation bubble downstream of the step.

The global energy content is seen to decrease for increasing distances to the step, which is consistent with the evolution of the $C_{p_{rms}}$ levels reported in Fig. 21. The low frequency content is attenuated while the energy content around $St = 0.2$ is strengthened, as discussed above. Similar results are obtained for the larger Re_h but are not reported here for the sake of brevity.

Pressure spectra obtained far downstream ($x/h=6.45$) and for four different values of Re_h are reported in Fig. 30.

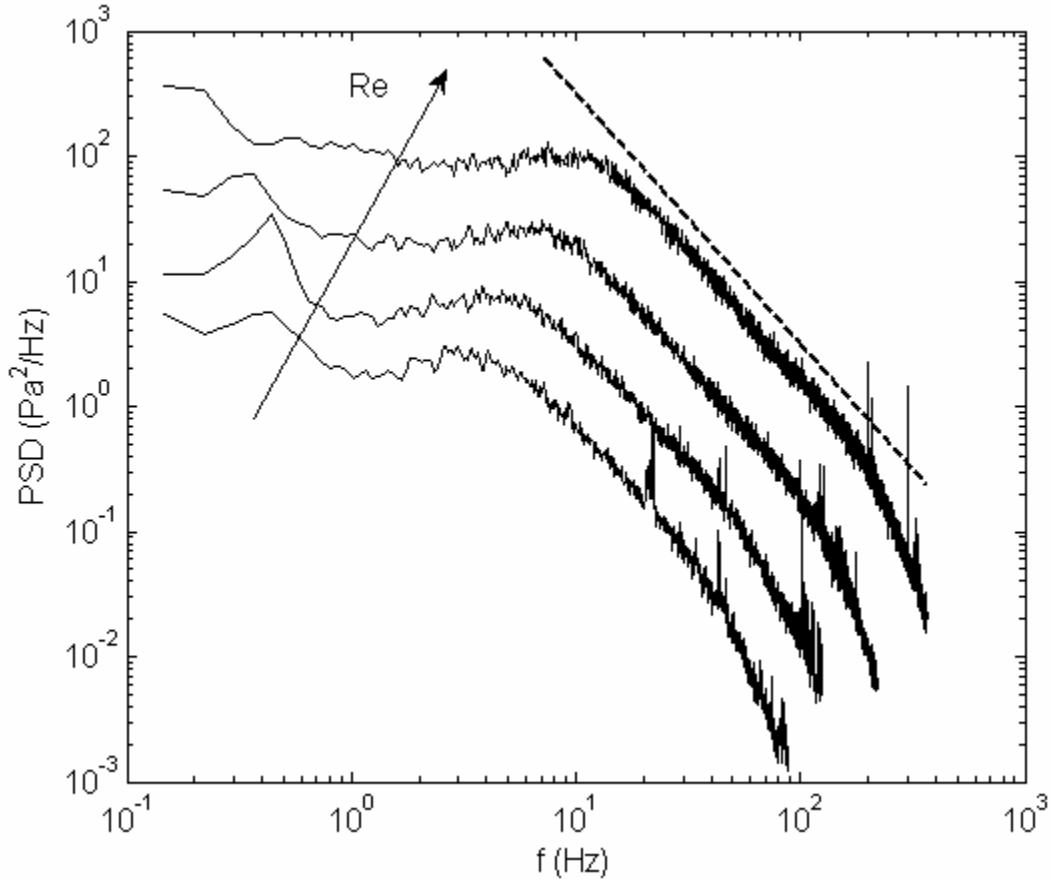


Figure 20 Pressure spectra obtained at $x/h=6.45$. Re_h varies from 8800 to 23 600 moving from bottom to top. The dashed straight line represents a power law with exponent of -2 .

The selected position is beyond the mean reattachment point of the recirculation region. The power spectra are reported in dimensional form to clearly outline the broadband increase of energy with Re_h . Moreover, regardless of the free stream velocity magnitude and in agreement with observations reported in Leclercq et al. 2001, all the power spectra exhibit a power-law decay with an exponent close to -2 (represented by the dashed line on the plot), which is still far from the -1 exponent expected for equilibrium TBL with no pressure gradients. Hence, even far downstream of the step, the boundary layer has not recovered its equilibrium state since the effects of the separation region are still

relevant. In this respect, Castro & Epick have shown that, downstream of the separated region generated by a blunt flat plate, the turbulence structure has not recovered the equilibrium conditions even 70 boundary-layer thicknesses after the separation point. A similar conclusion was reached by Song et al., who noticed that the outer layer recovery was quite slow with respect to the inner layer evolution.

Further insight is reached from a time-domain analysis based upon the computation of cross-correlations between any two transducers. It must be stressed that, despite the decontamination procedure applied to the power spectra, the acoustic background noise can not be completely cancelled from the time signals and thus the cross-correlations may be contaminated by spurious effects. However, it can be argued that the background noise is uncorrelated with the actual physical signals and thus its effects on the cross-correlations should not be significant. Based on the resulting time lag and on the distance between the selected transducers, it is then possible to determine the mean convection velocity U_c . A sample result is shown in Fig. 31, which represents the normalized cross-correlation coefficients (ρ_{12}) computed between two consecutive pressure transducers located upstream of the step and for three different Re_h . Because U_c is associated to the propagation of hydrodynamic pressure perturbations, the time lag is inversely proportional to the free stream velocity, with U_c being a fraction of this latter. The low amplitude oscillations observed in the cross-correlations are believed to have a physical origin.

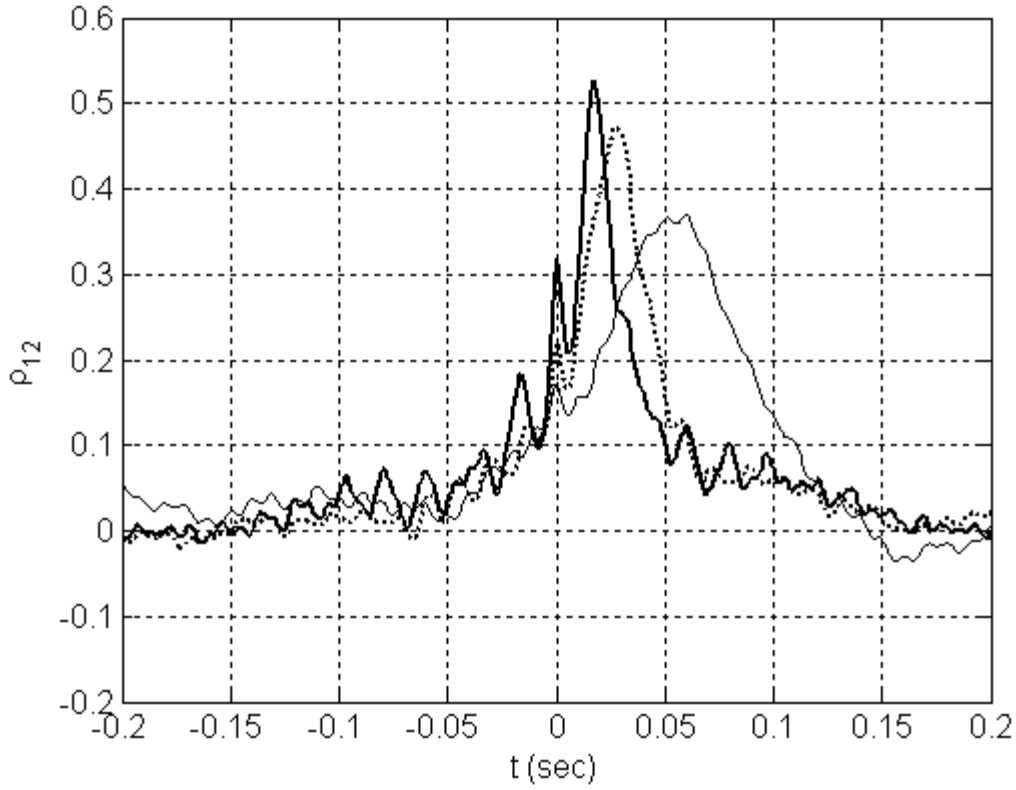


Figure 21 Examples of cross-correlation coefficients computed between two consecutive transducers for three different mean velocities. The solid bold line corresponds to $U_0 = 1.5$ m / s, the dashed line corresponds to $U_0 = 1$ m / s, and the solid line corresponds to $U_0 = 0.5$ m/s. The transducer pair is located upstream of the step, and the separation distance between the transducers is 15 mm. The first transducer of the pair in the longitudinal direction is at $-5.6h$ from the step.

They are most probably related to the characteristic size of the structures along the longitudinal direction. We also observe in Fig. 31 that the width of the main peak of the cross-correlation function decreases with increasing Reynolds number Re_h . Because this width is correlated to the size of the coherent structures present in the outer part of the TBL, we can conjecture that this size varies inversely with the upstream velocity. This result is consistent with the spectral analysis performed above, where the range corresponding to large scale structures (decay law with exponent -1) was found to extend more and more

into smaller wavenumber regions when increasing the Reynolds number. The size of the structures acts as a low-pass spatial filter that smoothes out the cross-correlation function as the size increases. For $U_0=1.5$ m/s, the secondary peaks correspond indeed to higher harmonics of the main correlation peak. Further analyses with the aid of the PIV realizations are in due course to clarify this point. In any case, as far as the evaluation of the hydrodynamic convection velocity is concerned, the oscillations are not relevant since their amplitude is much smaller than the cross-correlation main peaks. In order to verify the robustness of the convection velocity evaluation, cross-correlations between upstream transducers having different streamwise separations have been computed for a fixed free stream velocity, see Fig. 32.

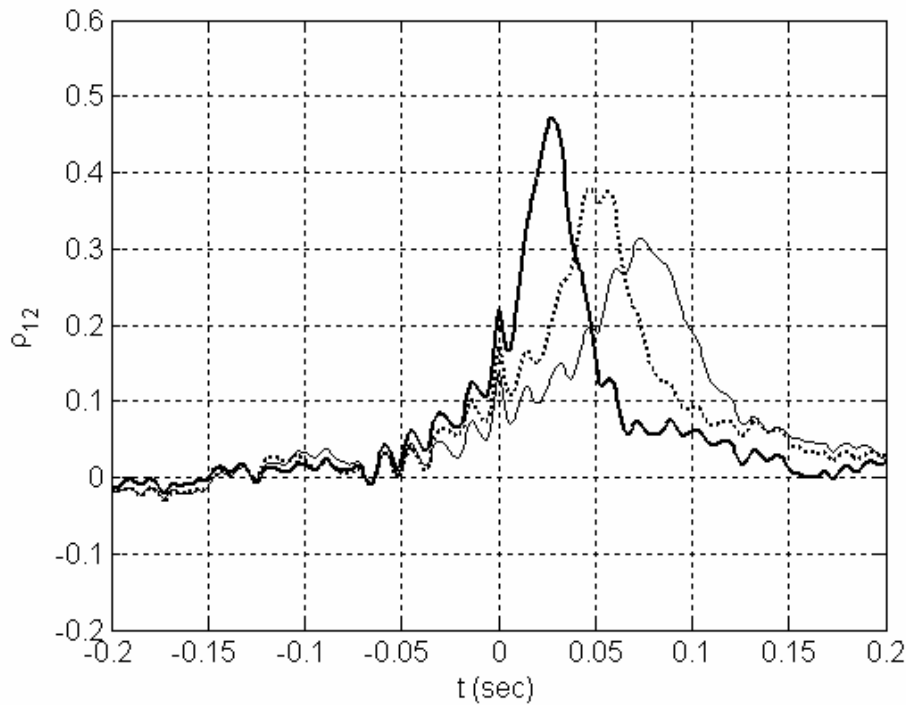


Figure 22 Same as the previous plot but for fixed Re_h ($U_\infty = 1$ m/s) and different separations: the solid line corresponds to a separation of 45 mm, the dashed line corresponds to 30 mm, and the solid bold line corresponds to 15 mm. The first transducer of the pairs in the longitudinal direction is at $-5.6h$ from the step.

As expected, the time shift associated to the largest cross-correlation peak is directly proportional to the separation distance between the transducers used for the calculation. Note that the peak width increases with increasing time lags. In other terms, the size of the structures in the outer part of the TBL increases as they approach the step discontinuity, thus giving a further verification of the spectral analysis discussed before (see Fig. 27). When the transducer pair is very close to the step, e.g. located inside the upstream separation bubble, a rather different behaviour is observed.

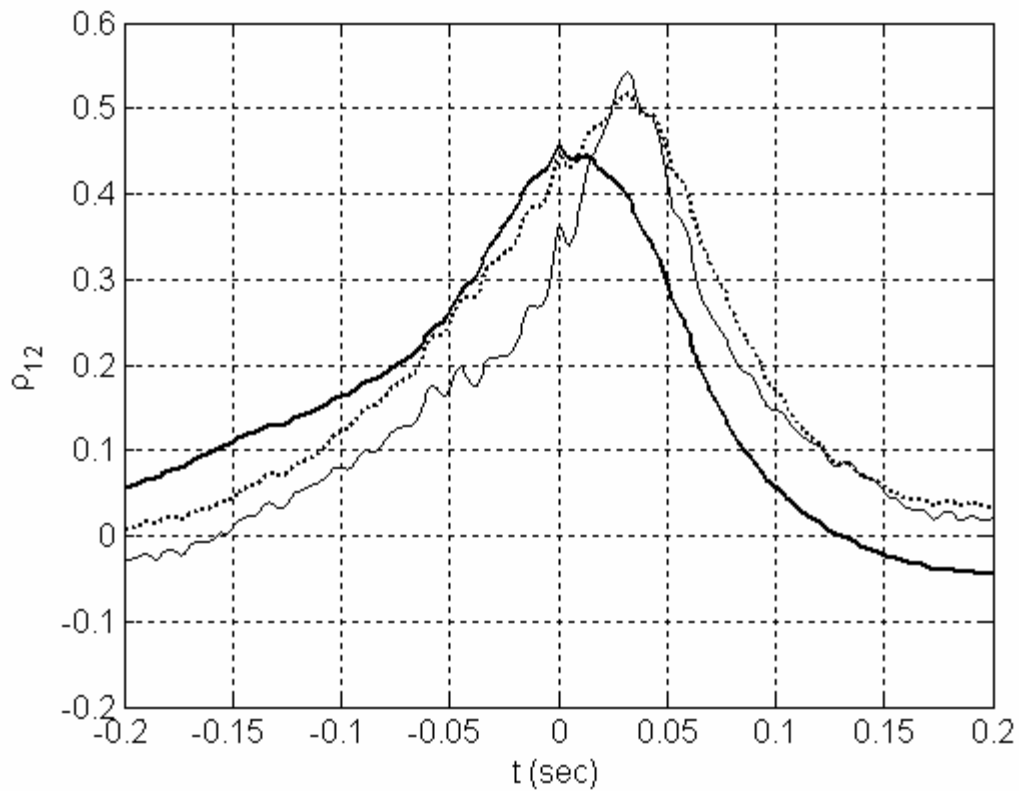


Figure 23 Same as the previous plot at fixed $Re_h(U_\infty=1 \text{ m/s})$, fixed separations (15 mm), but different distances from the step in the separated region upstream of it. The first transducer of the pairs in the longitudinal direction is at $-1.1h$ for the solid bold line, at $-1.85h$ for the dashed line, and at $-2.6h$ for the solid line.

The examples reported in Fig. 33 show that the effect of the large-scale, low-frequency shear layer unsteadiness due to the flow separation becomes dominant closer to the step. Indeed, the shear layer flapping produces in-phase pressure fluctuations, which lead to a close-to-zero time-shift. Furthermore, it is observed that the large-scale nature characterizing the flow structures in this region translates into a wide correlation peak, which is consistent with the spectral behaviour in the low frequency range outlined before (see Fig.27) .

Similar outcomes are reached for different transducer pairs as well as for different flow conditions, however the results are not reported here for the sake of conciseness.

For the downstream section of the flow, we report in Fig. 34 examples of cross-correlations computed for the highest Re_h , for a fixed separation between transducers and for different distances from the step. Other authors have documented similar findings in the re-attachment region downstream of separated flows. In contrast with the upstream results discussed above, the secondary periodic oscillations are no longer observed since the coherent structures, which are sources of the -1 decay exponent, are not present inside the re-circulation bubble. Besides, it is found that the time shift corresponding to the cross-correlation peak decreases for increasing distances to the geometrical discontinuity, which points out to a net increase of the convection velocity. In Fig.35, we report the hydrodynamic convection velocities U_c recorded along the flow direction for three Re_h . U_c is calculated using the time lag estimated from the cross-correlation function computed between pressure signals from adjacent locations (separation is $0.75h=15$ mm).

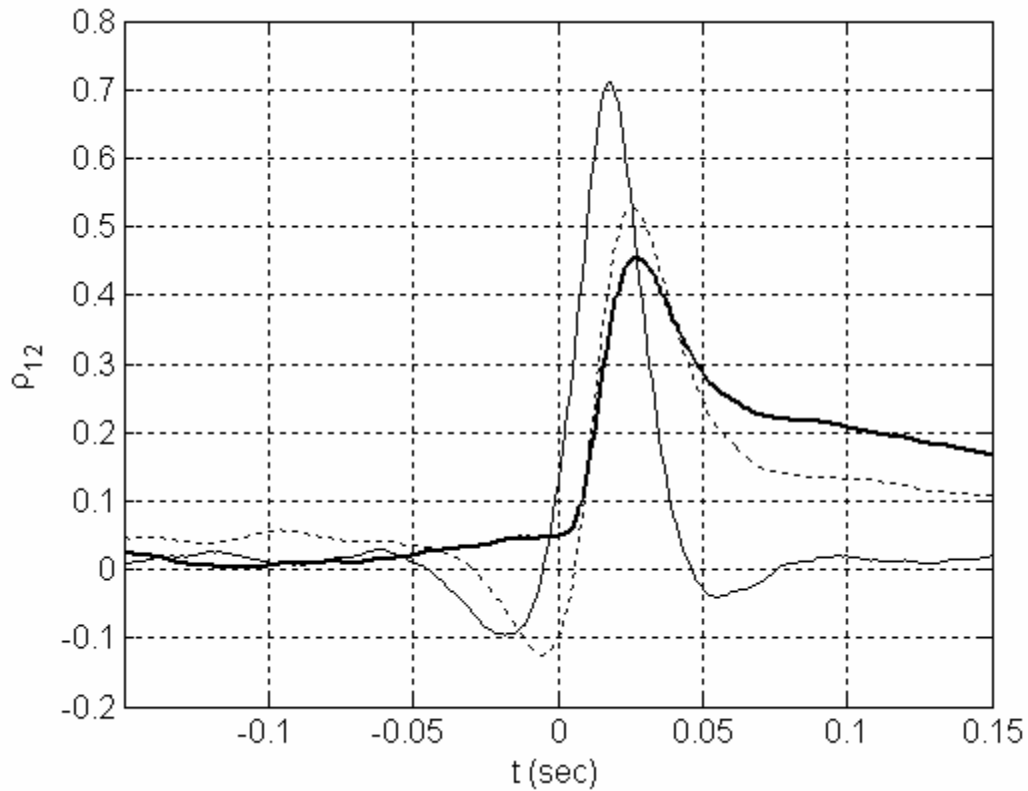


Figure 24 Cross correlations computed downstream of the step at $Re_h = 26\,300$ for fixed transducer separation (15 mm) and different distances from the step: the first transducer of the pairs in the longitudinal direction is at $0.45h$ for the solid bold line, at $1.2h$ for the dashed line, and at $4.2h$ for the solid lines.

Upstream of the step, the convection-to-free stream velocity ratio is within the range 0.5-0.7, remaining fairly constant in terms of the distance to the step, but significantly influenced by Re_h . One possible interpretation to this point lies in the fact that, with increasing speed, the sources of wall pressure are originating from deeper in the boundary layer, thus closer to the wall where the mean flow speed is lower. In the region downstream of the step, the ratio is approximately constant with Re_h and increases with the distance to the step from 0.4 to about 0.7, which is in agreement with results obtained in similar flow configurations.

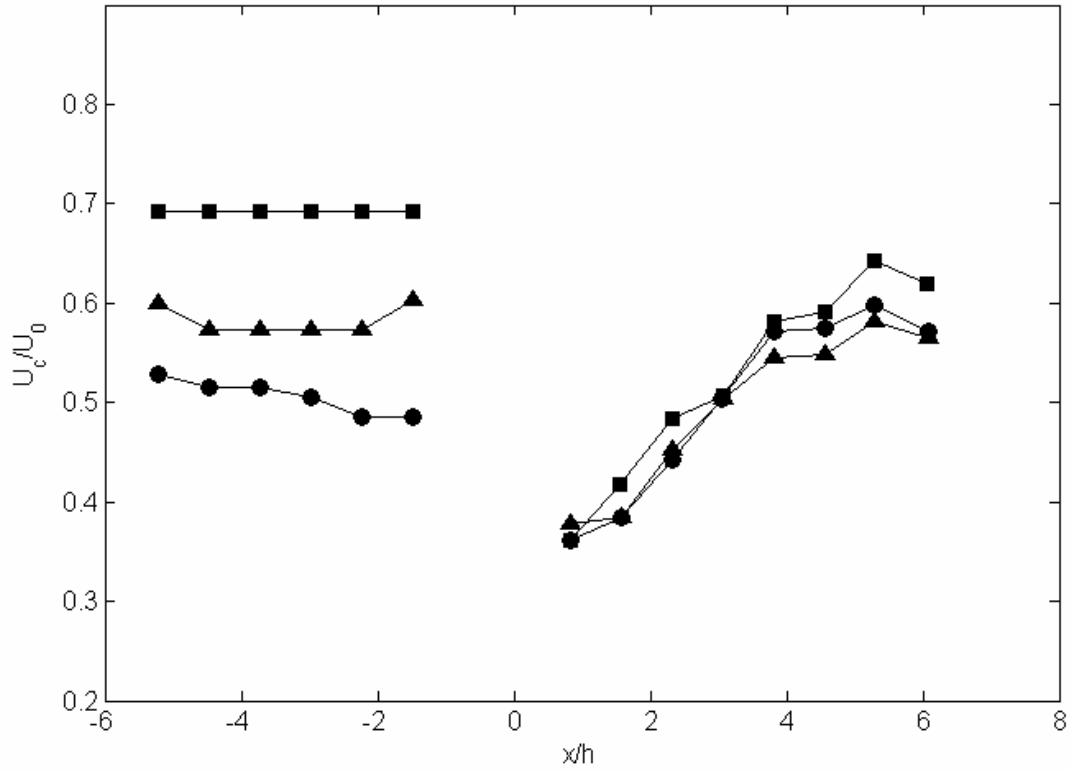


Figure 25 Convection velocities measured upstream and downstream of the step normalized with respect to the free stream velocity magnitude. Square symbols correspond to $U_0=0.5$ m/s, triangles correspond to $U_0=1$ m/s, and circles correspond to $U_0=1.5$ m/s.

4.2.2 Pressure/velocity correlations

A set of simultaneous wall pressure/time-resolved PIV acquisitions has been carried out at $Re_h=17600$, in the region downstream of the step. Through the computation of temporal cross-correlations between the velocity and the pressure data, insightful information could be revealed, in particular about the low frequency modes associated with the motion of the large scale structures. In the plots discussed below, the cross-correlation time scales are reported in a non-dimensional form, denoted as t^* and obtained multiplying t by U/h , so that

they can be directly compared to the Strouhal numbers used in the Fourier spectra representations of the previous section.

The cross-correlation is computed between the pressure signal from a selected transducer and the horizontal component of the velocity field extracted from the PIV time sequence. Since the PIV dataset is a two-dimensional vector field that extends along the streamwise direction (x-axis) and along the normal to the wall (y-axis), the cross-correlation dataset is itself a three-dimensional array comprising two spatial and one temporal dimension. The time histories of the velocity data were extracted from the PIV measurements on 30 equidistant positions along the y-direction from 0 to 1.6h and at a number of longitudinal locations extending from x=0 to x=3.5h. Previous to the cross-correlation operation, both the velocity and the pressure signals have been low-pass filtered at a cut-off frequency of 30Hz in order to remove spurious fluctuations.

From the analytical viewpoint, the time-correlation of the wall pressure fluctuations and the velocity signals can be defined as follows:

$$\rho_{p'v'}(x, y, \tau) = \frac{\overline{p'(x_{trans}, 0, t) \cdot v'(x, y, t + \tau)}}{\sqrt{\overline{p'^2(x_{trans}, 0, t)}} \cdot \sqrt{\overline{v'^2(x, y, t + \tau)}}}$$

with $0 \leq y \leq 1.6h$, $0 \leq x \leq 3.5h$, and $x_{trans} = 1.2h, 1.95h$ and $2.7h$ denoting the position of the selected pressure transducer.

Figure 36 represents the iso-contours of the pressure-velocity correlation coefficient for a number of locations along the streamwise direction, for the three selected wall pressure transducers (indicated by the black arrows). The

correlation maps show positive levels in correspondence of the recirculation bubble, with a steady increase of intensity from the front to the re-attachment zone, and a fast attenuation downstream. Slices of the velocity-pressure 3-D correlation map have been extracted and reported in Figs 37 and 38 which reveal features of particular interest. The cases reported in Fig. 37 represent the correlation maps between the pressure obtained from the transducer located at $x_{\text{trans}}=1.2h$, which is inside the recirculation bubble, and vertical profiles of the horizontal component of the velocity, placed at three streamwise locations. Significant positive correlation is found inside the recirculation bubble, as seen in the first two plots, whereas the correlation levels outside the bubble are essentially negative. Interestingly, the first two cases are also characterized by a seemingly periodic occurrence of maxima along the temporal axis, which can be interpreted as the signature of large scale structures that induce strong pressure fluctuations at the wall. The reference time of this motion, determined qualitatively from the temporal separation between successive correlation peaks, is around $t^*=5$. This time scale corresponds to a Strouhal number $St=0.2$ close to that observed in Largeau et al. 2007, and that can be physically ascribed to the effect induced by shear layer structures shed from the step front, advected over the recirculation bubble and further downstream close to the wall. It is also interesting to note that a positive time lag is observed for the first maximum of the pressure-velocity correlation at $y/h \approx 0.5$. This time lag is of about $t^*=1$ for the upper plot and of about $t^*=1.5$ for the mid one. Taking into account the magnitude of the mean velocity U used to normalize the time axis and the axial distance between the pressure transducers and the velocity line, a convection

velocity can be computed. It is found that the time delay of the first positive peak corresponds to a convection velocity that is about $0.3U$, in reasonable agreement with the findings of Fig.36 in the region downstream of the step..

For $y/h > 0.5$, i.e. outside the re-circulation bubble, the correlation amplitude weakens drastically, thus indicating that these quasi-periodic structures are a characteristic pattern of the flow near the recirculation bubble. Similar results are obtained with a pressure transducer placed slightly downstream at $x/h = 1.95$, as shown in Fig. 38.

It is finally stressed that the existence of a quasi-periodic motion due to the passage of large scale structures has been confirmed by the analysis of the Fourier frequency spectra of the velocity signals retrieved from the time-resolved PIV database. Due to the limited resolution of the PIV time series, the results are only qualitative and thus are not reported therein.

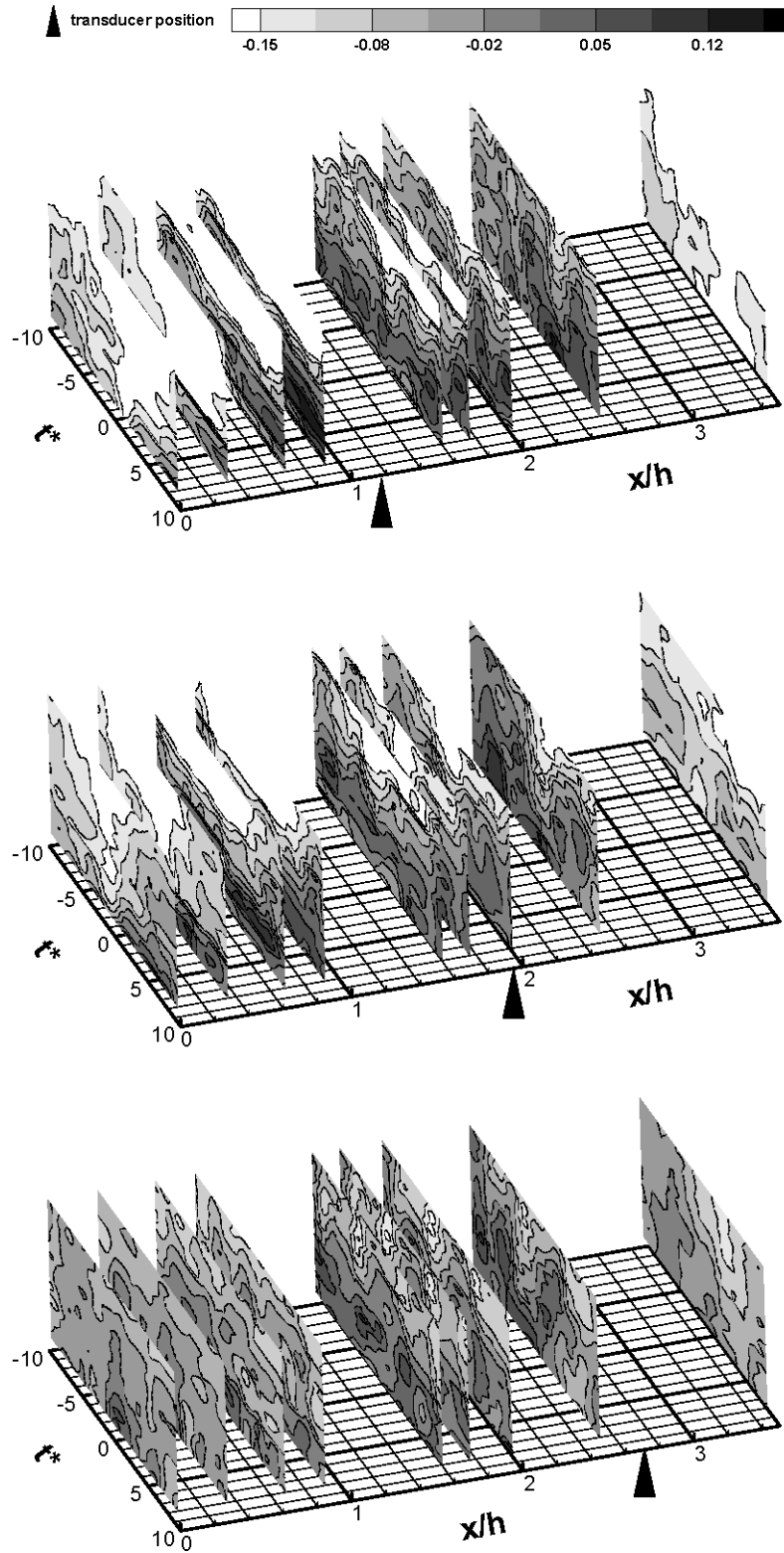


Figure 26 Three-dimensional view of the velocity-pressure correlation for the transducer positions $x_{trans}=1.2h$ (top), $1.95h$ (middle), and $2.7h$ (bottom).

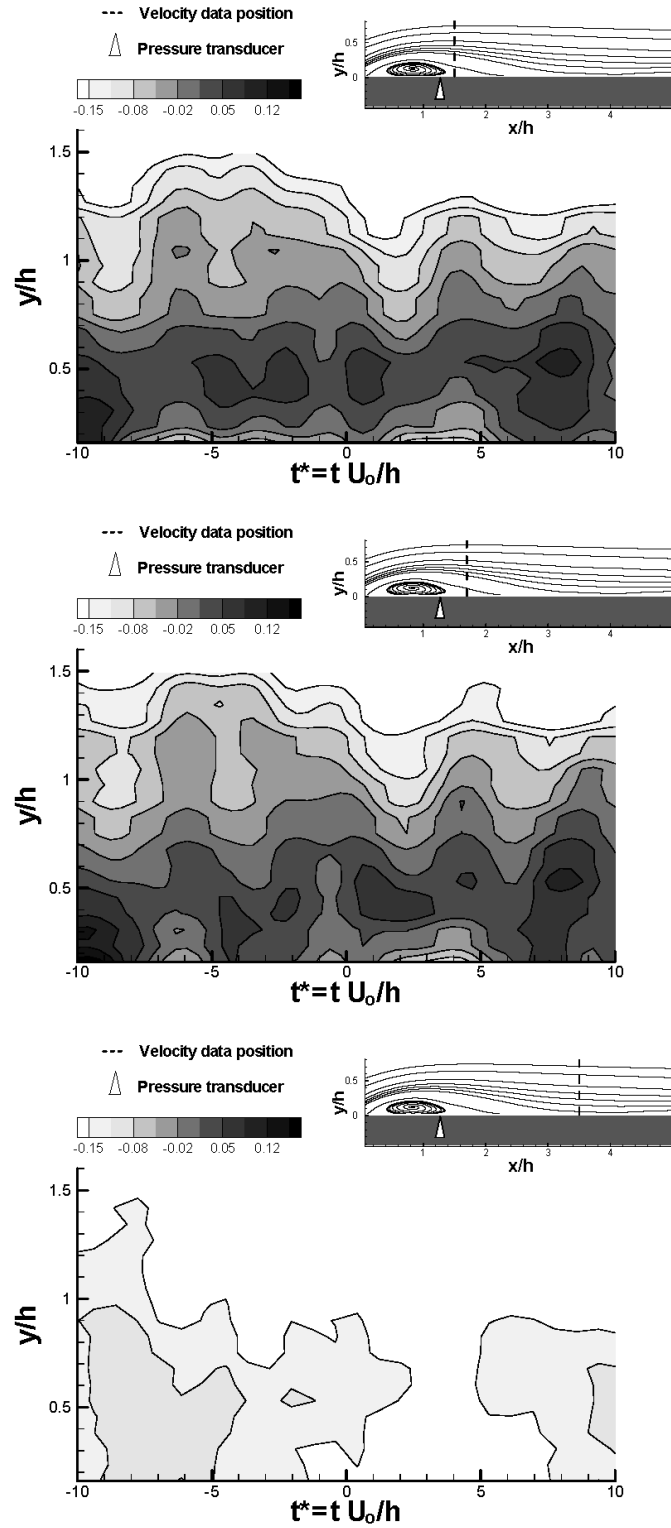


Figure 27 Two-dimensional view of the velocity-pressure correlation for the transducer positions $x_{trans} = 1.2h$ at the longitudinal stations $x = 1.5h$ (top), $x = 1.7h$ (middle), and $x = 3.5h$ (bottom).

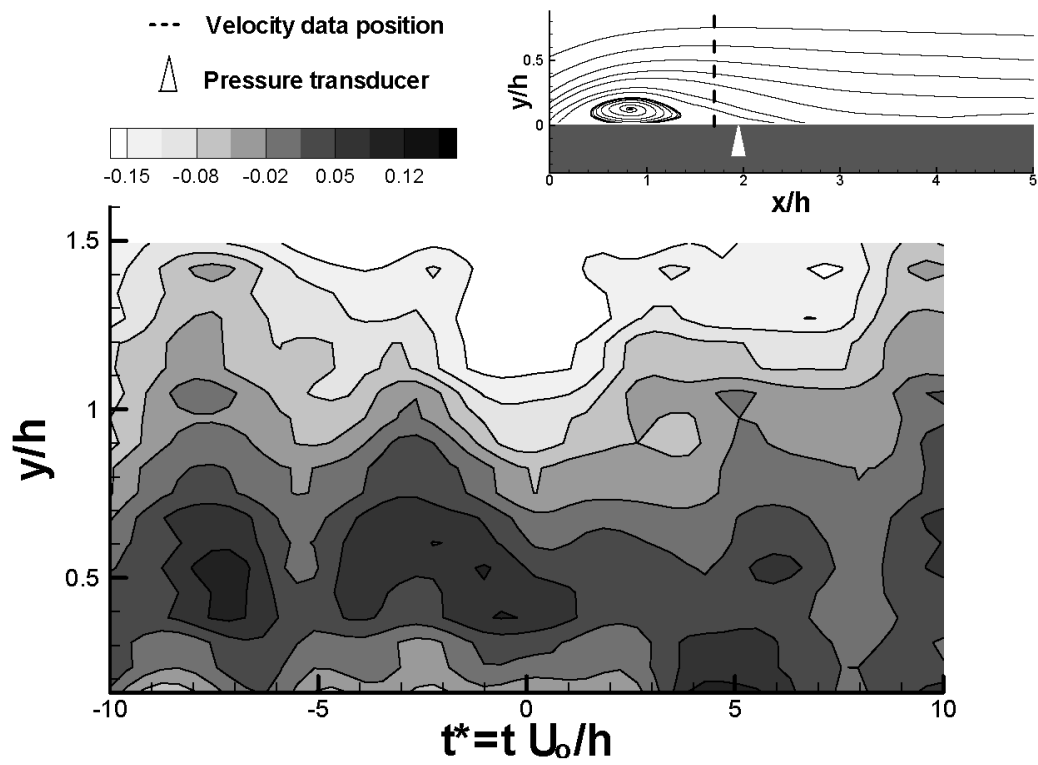


Figure 28 Two-dimensional view of the velocity-pressure correlation for the transducer position

$x_{trans} = 1.95h$ at the longitudinal station $x = 1.7h$

5 Conclusion

5.1 Attached TBL

In this thesis, a TBL at quite large Reynolds numbers is investigated experimentally by means of the PIV technique. The use of a high-speed camera for image acquisition allows obtaining both statistical moments (by using almost uncorrelated images at large time separation) and evolution of instantaneous velocity fields (by using close correlated images at small time separations, i.e. a few Taylor microscales). The obtained temporal (0.2 wall time units) and spatial resolution (10 wall units), although not sufficient to describe the entire spectrum of scales in the TBL, seems to be high enough to characterize the improperly (as demonstrated by present data) so-called logarithmic region, i.e. the region for y^+ between 30 and 2000 (in any case dependent on the Reynolds number).

The first objective of the thesis is to consider average velocity profiles in a direction orthogonal to the wall in order to determine which of the proposed “laws of the wall” is suitable to describe the behaviour of data at such high Reynolds numbers. In addition to this, it is important to investigate if some Reynolds number effect is present. The careful analysis of the present data, aiming to amplify differences among data and models by using velocity gradient profiles, reveals that the logarithmic law of the wall is not followed anywhere in the boundary layer (at least for $y^+ < 4000$) except possibly for very small sub-intervals. On the other hand, the power law and parametric models seem to well describe data behaviour, the former for $100 < y^+ < 600$ (slightly dependent on

Reynolds number) whereas the latter even for smaller wall distances. It is rather important to consider that this conclusion is substantially independent of the values assigned to the parameters involved in all model laws of the wall.

The second objective of the thesis is to consider the relevance of the ‘coherent’ part of wall dynamics over the ‘non-coherent’ part. To do this, it is necessary to define a priori what this means. So far, near-wall vortical structure eduction methods have to be used and compared: Reynolds decomposed fields, vorticity, velocity gradient tensor invariants and wavelets. Surprisingly, except for the very near-wall region ($y^+ < 30$, where vorticity-based methods are not able to detect vortices and where the high image noise makes velocity gradients difficult to be derived) the different methods agree reasonably in describing a common picture. Packets of vortices are generated along the same inclined direction (about 30°) in respect to the wall and convected by the streamwise velocity. The relevance of such packets over the entire wall dynamics is determined by looking at the detected vortex size probability distribution. The observation of a clear exponential tail over vortices larger than the average (which is almost equal to $1/10$ of the boundary layer displacement thickness) indicates that there is a hierarchical cascade among them. This is observed only for vortices larger than the average and not for those smaller (although there should be some effect due to resolution limitations). In particular, the experimentally determined coefficients suggest the formation of about seven ‘children’ vortices from each ‘parent’ one. In comparison to a pure noisy vector field (artificially generated), the relevance of the ‘non-coherent’ part is about $1/10$, thus indicating a

substantial contribution of the ‘coherent part’ to the near-wall dynamics. These results are almost independent of Reynolds number.

So far, in the framework of the present analysis, the questions raised in the ‘Introduction’ can find here partial answers:

(1) What is the dependence of the observed phenomena on Reynolds number?

The behaviours of both the wall-normal velocity profiles and wall dynamics are only slightly dependent on Reynolds number once proper scaling is assumed (friction velocity and average vortex size). A possible exception is given by the second-order statistical moments, and this can be further analyzed.

(2) What is the effective relevance of the coherent part in comparison to the entire TBL dynamics at high Reynolds numbers? There is a clear link among vortical structures formed in the TBL indicating the existence of a hierarchy (packets?). The relevance of the ‘coherent’ part seems to be 10 times larger than in the case of randomly distributed vortex size.

5.2 The FFS behaviour

Wall pressure fluctuations and velocity fields have been measured upstream and downstream of a forward facing step model installed inside a large scale recirculating water tunnel. Measurements have been conducted at different Reynolds numbers both in the region upstream and downstream of the step front. In some limited cases, PIV images and wall pressure data have been acquired simultaneously and temporal pressure/velocity cross-correlations have been computed.

The time-resolved PIV results have helped us to characterize the overall flow physics as well as clearly localize the separated regions upstream and downstream of the vertical side of the step. It has been observed that the Reynolds number mostly affects the size and intensity of the recirculation region downstream of the vertical side of the step whereas the upstream region remains more stable. Also the PDFs of the wall pressure signals exhibit close-to-universal shapes in the region upstream of the step front, whereas the PDF shapes in the downstream section are strongly affected by the flow conditions. In the region upstream of the step, the wall pressure PDFs are skewed under the effect of predominantly positive pressure surges, hence clearly departing from the case of homogeneous and isotropic turbulence.

The wall pressure cross-correlation coefficients not only enabled the determination of the propagation velocity of the hydrodynamic perturbations, but also revealed the signature of the shear layer unsteadiness and of the large scale re-circulation region in the region upstream of the step. The wall pressure frequency spectra upstream of the step revealed the coexistence of two power-

law decays with exponents typical of equilibrium TBL (f^{-1}) and separated regions ($f^{-7/3}$). The cross-over between the two scalings has been observed to occur at a constant Strouhal number of about 0.2. Much steeper decay laws are observed along the region downstream of the step, even though a tendency towards the behaviour expected in equilibrium conditions is also observed further downstream.

The overall Cp_{rms} increases in magnitude in the vicinity of the geometrical discontinuity and displays a maximum in the region located around 2 step's heights downstream of the vertical side of the step. This position coincides with the average location of the reattachment point. This behaviour is in contrast with acoustic results reported in literature which identify the separated region upstream of the step as the major noise source. A possible reason of this behaviour can be related to the rapid acceleration of the flow as it passes over the step. A Lighthill acoustic analogy applied to the flow field of a forward facing step would most likely show that the step face is the region of strongest acoustic radiation since this is the location where the shape changes most rapidly.

Further analyses are currently undertaken by the authors to clarify this issue through a numerical simulation in order to establish the properties of the wall pressure fluctuations along the vertical side of the step, which is an information quite difficult to obtain experimentally.

The time analysis of pressure-velocity correlations indicated that, in the region downstream of the front of the step, the surface pressure fluctuations are mostly related to large scale vortex structures advected in the shear layer, in agreement with literature results. The predominant effect revealed by the cross-

correlations is the quasi-periodic nature of the shedding, for which a non-dimensional period has been established. The presence of secondary structures generated in the vicinity of the reattachment position and close to the wall has also been documented. The typical frequency of the main structures is found to correspond to a characteristic Strouhal number of around 0.2, which is consistent with the typical shear layer time-scale commonly reported in literature.

6 References

1. W.K. Blake, Mechanics of flow induced sound and vibrations, Appl. Math. and Mech., Acad. Press Inc., Orlando (FL) (1986).
2. M.K. Bull, "Wall pressure fluctuations beneath turbulent layer: some reflections on forty years of research", J. Sound Vibr. **190**, 299-315 (1996).
3. Y. Na and P. Moin, "The structure of wall-pressure fluctuations in turbulent boundary layers with adverse pressure gradient and separation", J. Fluid Mech. **377**, 347-373 (1998).
4. R.L. Simpson, "Turbulent boundary-layer separation", Annu. Rev. Fluid Mech. **21**, 205-234 (1989).
5. M. Kiya and K. Sasaki, "Structure of a turbulent separation bubble", J. Fluid Mech. **137**, 83-113 (1983).
6. M. Kiya and K. Sasaki, "Structure of large-scale vortices and unsteady reverse flow in the reattaching zone of a turbulent separation bubble", J. Fluid Mech. **154**, 463 - 491 (1985).
7. L.M. Hudy, A.M. Naguib and W.M. Humphreys Jr, "Wall-pressure-array measurements beneath a separating/reattaching flow region", Phys. Fluids **15**, 706-717 (2003).
8. S. Song, D.B. DeGraaff and J.K. Eaton, "Experimental study of a separating, reattaching, and redeveloping flow over a smoothly contoured ramp", Intl. J. Heat Fl. Flow, **21**, 512-519 (2000).

9. J. Kim, and H.J. Sung, "Wall pressure fluctuations and flow-induced noise in a turbulent boundary layer over a bump", *J. Fluid Mech.* **558**, 79 – 102 (2006).
10. H. Stuer, A. Gyr and W. Kinzelbach, "Laminar separation on a forward facing step", *Eur. J. Mech. B/Fluids* **18**, 675–692 (1998).
11. J.F. Largeau and V. Moriniere, "Wall pressure fluctuations and topology in separated flows over a forward-facing step", *Exp. Fluids* **42**, 21–40 (2007).
12. B.M. Efimtsov, N.M. Kozlov, S.V. Kravchenko and A.O. Anderson, "Wall Pressure Fluctuation Spectra at Small Forward-Facing Step", *Proceedings of the 5th AIAA/CEAS Aeroacoustics Conference - AIAA paper 99-1964*, Bellevue, WA, USA (1999).
13. D.J.J. Leclercq, M.C. Jacob, A. Louisot and C. Talotte, "Forward-backward Facing Step Pair: aerodynamic flow, wall pressure and acoustic characterisation", *Proceedings of the 7th AIAA/CEAS Aeroacoustics Conference - AIAA paper 2001-1249*, Maastricht, The Netherlands (2001).
14. Y. Addad, D. Laurence, C. Talotte, and M.C. Jacob, "Large Eddy Simulation of a Forward-Backward Facing Step for Acoustic Source Identification", *Intl. J. Heat Fl. Flow* **24**, 562-571, (2003).
15. R. Camussi, G. Guj and A. Ragni, "Wall pressure fluctuations induced by turbulent boundary layers over surface discontinuities", *J. Sound Vibr.* **294**, 177–204 (2006).

16. R. Camussi, G. Guj, A. Di Marco and A. Ragni, "Propagation of wall pressure perturbations in a large aspect-ratio shallow cavity", *Exp. Fluids*, **40**, 612-620 (2006).
17. C. Hoarau, J. Borée, J. Laumonier, and Y. Gervais, "Analysis of the wall pressure trace downstream of a separated region using extended proper orthogonal decomposition", *Phys. Fluids* **18**, 055107-1 055107-12 (2006).
18. W.D. Moss and S. Baker, "Re-circulating flows associated with two-dimensional steps", *Aeronautical Quarterly* **31**, 151-172 (1980).
19. R. Camussi and F. Di Felice, "Statistical properties of large scale spanwise structures in zero pressure gradient turbulent boundary layers", *Phys. Fluids* **18**, 035108-1 035108-16 (2006).
20. M. K. Bull, "Wall-pressure fluctuations associated with subsonic turbulent boundary layer flow", *J. Fluid Mech.* **28**, 719-754 (1967).
21. G.M. Corcos, "The resolution of pressures in turbulence", *J. Acoust. Soc. Am.* **35**, 192-199 (1963).
22. F. Scarano, "Iterative image deformation methods in PIV", *Meas. Sci. Tech.* **13**, R1-R19 (2002).
23. T.M. Farabee and M.J. Casarella, "Measurements of fluctuating wall pressure for separated/reattached boundary layer flows", *Journal of Vibration, Acoustics, Stress and Reliability in Design* **108**, 301-307 (1986).
24. N.J. Cherry, R. Hillier and M.E.M.P. Latour, "Unsteady measurements in a separated and reattaching flow", *J. Fluid Mech.* **144**, 13 - 46 (1984).

25. A. Steinwolf and S.A. Rizzi, "Non-Gaussian Analysis of Turbulent Boundary Layer Fluctuating Pressure on Aircraft Skin Panels", J. Aircraft **43**, 1662-1675 (2006).
26. M. Carley and J.A. Fitzpatrick, "Spectral conditioning of propeller noise from broadband sources", J. Sound Vibr. **238**, 31-49 (2000).
27. T.M. Farabee and M.J. Casarella, M.J., "Spectral features of wall pressure fluctuations beneath turbulent boundary layers", Phys. Fluids A **3**, 2410-2420 (1991).
28. P. Bradshaw, "Inactive motion and pressure fluctuations in turbulent boundary layers", J. Fluid Mech. **30**, 241-258 (1967).
29. M.C. Goody, R.L. Simpson and C.J. Chesnakas, "Separated flow surface pressure fluctuations and pressure-velocity correlations on prolate spheroid", AIAA J **38**, 266-274 (2000).
30. G. K. Batchelor, *The Theory of Homogeneous Turbulence*, Cambridge Univ. Press. (1953).
31. I. Lee and H.J. Sung, "Multiple-arrayed pressure measurement for investigation of the unsteady flow structure of a reattaching shear layer", J. Fluid Mech. **463**, 377-402 (2002).
32. I.P. Castro and E. Epik, "Boundary layer development after a separated region", J. Fluid Mech. **374**, 91 - 116 (1998).
33. H.G.K. Schlichting, *Boundary Layer Theory*. 8th Revised Edition, Berlin, Heidelberg, Springer-Verlag, 2000.

34. G.I. Barenblatt, Scaling laws for fully developed turbulent shear flows. Part1. Basic hypotheses and analysis, J. Fluid Mech. 248 (1993), pp. 513–520.
35. G.I. Barenblatt and V.M. Prostokishin, Scaling laws for fully developed turbulent shear flows. Part 2. Processing of experimental data, J. Fluid Mech. 248 (1993), pp. 521–529.
36. M.V.Zagarola, A.E.Perry and A.J.Smits, Log laws or power laws: The scaling in the overlap region, Phys. Fluids 9 (1997), pp. 2094–2100.
37. M.V. Zagarola and A.J. Smits, A new mean velocity scaling for turbulent boundary layers, ASME FEDSM '98, Washington, DC, June 21–25 (1998), pp. 1–6.
38. M.V. Zagarola and A.J. Smits, Mean-flow scaling of turbulent pipe flow, J. Fluid Mech. 373 (1998), pp. 33–79.
39. J.F.Morrison, B.J. McKeon, W. Jiang, and A.J. Smits, Scaling of the streamwise velocity component in turbulent pipe flow, J. Fluid Mech. 508 (2004), pp. 99–131.
40. M.H.Buschmann and M.Gad el Hak, Generalized logarithmic law and its consequences, AIAA J. 41(1) (2003), pp. 40–48.
41. M.H.Buschmann and M.Gad el Hak, Debate concerning the mean velocity profile of a turbulent boundary layer, AIAA J. 41(4) (2003), pp. 565–572.
42. I. Procaccia and K.R. Sreenivasan, The state of the art in hydrodynamic turbulence: Past successes and future challenges, Phys. D Nonlin. Phenom. 237 (2008), pp. 2167–2183.

43. V.S. L'vov, I. Procaccia, and R. Oleksii, Universal model of finite Reynolds number turbulent flow in channels and pipes, *Phys. Rev. Lett.* 100(5) (2008), pp. 054504.
44. S.K. Robinson, Coherent motion in the turbulent boundary layer, *Annu. Rev. Fluid Mech.* 23 (1991), pp. 601–639.
45. R.J. Adrian, C.D. Meinhart, and C.D. Tomkins, Vortex organization in the outer region of the turbulent boundary layer, *J. Fluid Mech.* 422 (2000), pp. 1–54.
46. C.D. Tomkins and R.J. Adrian, Spanwise structure and scale growth in turbulent boundary layers, *J. Fluid Mech.* 490 (2003), pp. 37–74.
47. J. Jeong, F. Hussain, W. Schoppa, and J. Kim, Coherent structure near the wall in a turbulent channel flow, *J. Fluid Mech.* 332 (1997), pp. 185–214.
48. A.E. Perry and I. Marusic, A wall-wake model for the turbulence structure of boundary layers. Parts 1 and 2, *J. Fluid Mech.* 298 (1995), pp. 361–407.
49. R. Camussi, Coherent structure identification from wavelet analysis of particle image velocimetry data, *Exp. Fluids* 32 (2002), pp. 76–86.
50. H.T. Huang, H.F. Fielder, and J.J. Wang, Limitation and improvement of PIV; part II: Particle Image Distortion, a novel technique, *Exp. Fluids* 15 (1993), pp. 263–273.
51. F. Scarano and M.L. Riethmuller, Advances in iterative multigrid PIV image processing, *Exp. Fluids* 27 (Special issue) (2000), pp. S51–S60.
52. F. Scarano, Iterative image deformation methods in PIV, *Meas. Sci. Tech.* 13(2002), pp. 1–19.

53. F. Pereira, A. Ciarravano, F. Di Felice, and G.P. Romano, Adaptive multi-frame PIV, XII International Symposium on Applications of Laser Anemometry to Fluid Mechanics, Lisbon, 2004
54. J.C. Klewicki and R.E. Falco, On accurately measuring statistics associated with small-scale structure in turbulent boundary layers using hot-wire probes, *J. Fluid Mech.* 219 (1990), pp. 119–142.
55. P.R. Spalart, Direct simulation of a turbulent boundary layer up to $R = 1410$, *J. Fluid Mech.* 187 (1988), pp. 61–98.
56. J.M. Osterlund, A.V. Johansson, H.M. Nagib, and M.H. Hites, A note on the overlap region in turbulent boundary layers, *Phys. Fluids* 12 (2000), pp. 1–4.
57. W. Smith, Effect of Reynolds number on the structure of turbulent boundary layers, Rep. 1984-T, Department of Mechanical and Aerospace Engineering, Princeton University, Princeton, NJ, 1994.
58. J.C. Russ, *The Image Analysis Cookbook*, Boca Raton, FL, CRC Press, 2002, p. 238.
59. J. Jeong and F. Hussain, On the identification of a vortex, *J. Fluid Mech.* 285 (1995), pp. 69–94.
60. M. Farge, Wavelet transforms and their applications to turbulence, *Annu. Rev. Fluid Mech.* 24 (1992), pp. 395–457.
61. A. Zanon, F. Durst, and H.M. Nagib, Evaluating the law of the wall in two-dimensional fully developed turbulent channel flows, *Phys. Fluids* 15 (2003), pp. 3079–3089.

62. D.B. De Graaf and J.K. Eaton, Reynolds-number scaling of the flat-plate turbulent boundary layer, *J. Fluid Mech.* 422 (2000), pp. 319–346.
63. P. Bradshaw, 'Inactive' motion and pressure fluctuations in turbulent boundary layers, *J. Fluid Mech.* 30 (1967), pp. 241–258.
64. J.C.R. Hunt and J.F. Morrison, Eddy structure in turbulent boundary layers, *Eur. J. Mech.* 19 (2000), pp. 673–694.
65. G.P. Romano, Analysis of two-point velocity measurements in near-wall flows, *Exp. Fluids* 20 (1995), pp. 68–83.
66. J. Lin, J.P. Laval, J.M. Foucaut, and M. Stanislas, Quantitative characterization of coherent structures in the buffer layer of near-wall turbulence, *Exp. Fluids* 45 (2008), pp. 999–1014.
67. R.J. Adrian, Hairpin vortex organization in wall turbulence, *Phys. Fluids* 19 (2007), pp. 041301.
68. D.S. Dean and S.N. Majumdar, Extreme value statistics of hierarchically correlated variables: Deviation from Gumbel statistics and anomalous persistence, *Phys. Rev. E* 64 (2001), pp. 046121.